Investigating $^{15}N@C_{60}$ using pulsed EPR and the use of new techniques in resonator production

Michael O'Shaughnessy Gutierrez

Physics

Lancaster University

A dissertation submitted for the degree of

Physics MSc

February, 2026

Abstract

Improvements in timekeeping offer a wide range of benefits, and are of particular interest for global navigation satellite systems (GNSS). The accuracy and reliability of these can be dramatically improved with an improved receiver clock. A chip scale atomic clock (CSAC) could offer greatly improved performance when compared to current quartz oscillators. A CSAC is under investigation at Lancaster University, using $^{15}N@C_{60}$, this is a Nitrogen-15 atom trapped inside a fullerene cage, and shows great potential for use in a CSAC; it offers potential improvements in size, weight and power in comparison to other CSAC technologies, which are very important in making a CSAC feasible to use, especially in consumer electronics.

The Lancaster group's prototype clock has room for improvement. Firstly, an investigation into potential improvements in the resonator was conducted. Litz wire and 3D printed resonators were developed and tested, showing worse Q factors than currently used solenoid resonators. A 3D printed form for making new solenoid resonators was created, and improved the creation process of new solenoids. Clock stability is parametrised by Allan deviation, which measures the rate of drift of a clock; this has not yet been measured at the clock transition. Progress has been made towards this in the form of a measurement of T_2 relaxation time in $^{15}N@C_{60}$ at 60MHz. This was found to be $3.9 \pm 0.5\mu$s and $5 \pm 1\mu$s for 2.1mT and 2.0mT transitions respectively, giving frequency linewidths of $\delta f = 80 \pm 10$kHz (2.1mT) and $\delta f = 60 \pm 10$kHz (2.0mT). Taking these to be the clock transition linewidths, Allan deviation estimates of: $\sigma_y(\tau) = 2.2 \pm 0.3 \times 10^{-4}\tau^{1/2}$ for 2.1mT, and $\sigma_y(\tau) = 1.6 \pm 0.3 \times 10^{-4}\tau^{1/2}$ for 2.0mT, were calculated. Finally, an investigation into the signal-to-noise (S/N) ratio was carried out: the noise was found to be higher than theoretical levels, and did not reduce with averaging as much as expected. While the Allan deviation estimates are low, the issues with S/N ratio show clear potential for improvement in the setup, which may allow for a measurement of the linewidth to be made at the clock transition.

Contents

List of Tables and figures

Acknowledgements

There are too many people to thank them all individually; listed here are a few to whom I would like to give special thanks. Firstly, my supervisor Prof. Edward Laird, who gave me freedom enough to investigate how I wanted, while also being always ready to get into the nitty-gritty when I needed help. More generally I think Edward really shows how an academic should behave, a role model who will guide me for the rest of my time in academia.

Next I'd like to thank the people in the lab, particularly Sam Dicker, Patrick Steger, Scott Henderson and Doc. Edward Riordan: for being incredibly welcoming and always willing to lend a hand with everything even if wasn't related to their field, or even physics at all.

Special thanks to my friends from home who were always there to listen or give a hand, in particular Edward Heywood whose mind I bounced pretty much everything I did off.

Finally I'd like to thank my parents, who not only always believed in me but especially in my mum's case really pushed me to do the best I could; without them I don't think I'd have even chosen to come back to Physics.

Declaration

I declare that the work presented in this thesis is, to the best of my knowledge and belief, original and my own work. The material has not been submitted, either in whole or in part, for a degree at this, or any other university. This thesis does not exceed the maximum permitted word length of 35,000 words including appendices and footnotes, but excluding the bibliography. A rough estimate of the word count is: 14587

Michael O'Shaughnessy Gutierrez

Chapter 1

Introduction

1.1 Developments In Timekeeping

Timekeeping has been important throughout human history, facilitating society in many forms. This has never been more so the case than the present, where accurate timekeeping is relied on in most advanced technologies, particularly in global communications, global navigation satellite systems (GNSS), and in financial markets [1].

Accurate timekeeping requires a with consistent frequency; the first of these 'clocks' were sundials, measuring the passage of time using shadows from the sun and have existed since 1500 BCE [2]. However, the length of the day varying across a country and across a year makes coordinating or keeping consistent time with this method difficult. Several types of clocks offered a more consistent solution. One solution is the uniform flow of a material, i.e. sand or water, seen in the sand timers used by scholars and monks to time their studies [3]. Early mechanical clocks used periodic oscillations driven by springs or falling weights [4]. For example, the Verge and Foliot mechanism was used extensively, for example in many of the early clock towers built around Europe e.g. St Paul's Cathedral, Paris, Westminster [5]. While neither of these forms of timekeeping were terribly accurate [6] they made 'equal hours' possible, where the length of the day no longer varied, as it was no longer based on fluctuating cosmological observations [7].

Pendulum clocks were the next big advancement, providing much more accurate time than had existed beforehand [8]. These used the constant frequency of a pendulum to drive a gear and measure the passage of time. Within a decade of invention these offered a 30 fold increase in stability, from 300s of loss per day to 10s [9]. This meant that they were now reliable enough to be used in scientific experiments [10].

Although far more accurate than all previous clocks, they could not be used at sea for navigation because of the differing effects of gravity at different latitudes as well as the rocking and movement of the ship [11]. Latitude could be found using solar observation, but accurately determining longitude requires an accurate local time to to compare to the reference time. The first clock stable enough to be used for this was the marine chronometer, developed in 1735 by John Harrison; this clock rather than using a pendulum used springs to drive oscillation [11]. This provided huge benefit to marine navigation. The reference that these used was held at Greenwich and was so widespread that by late 19th century 70 percent of worlds shipping used Greenwich as their reference [12]. The use of Greenwich as a reference later spread to the rest of the UK once the electric telegraph was developed, providing a way of distributing it. This new capability, along with the growth of the national railway system providing a motivation for a national standard time, lead to the establishment of Greenwich Mean Time (GMT) [13].

The next major advancement in time-keeping was the development of quartz-based clocks, which exploited the piezoelectric property of quartz crystals: small mechanical stresses cause electric currents, and inversely small currents can cause flexing. These flexes can be driven by a current and have resonances, and due to the piezoelectric effect then produce currents in the crystal which can be measured. The resonant frequency depends primarily on the physical properties of the crystal [14]. This is typically chosen to be 32768Hz, which importantly is the first power of 2 above human hearing range, and can then be mixed down to a 1Hz signal which is used to drive the clock to tick [15]. Within 2 years of their development they were as accurate as the best pendulum clocks [16]. Alongside this quartz clocks offered miniaturization that simply was not possible with mechanical devices while maintaining their low cost and good accuracy. These factors have lead to quartz clocks being used in almost all types of modern electronics, with billions of quartz oscillators being produced annually [17].

While quartz clocks are quite accurate their frequency is still dependent on the physical properties of the crystal, alongside instabilities caused by ageing and temperature fluctuations [18]. An ideal clock standard would be based on something more fundamental. The most accurate clocks currently produced are atomic clocks, which represent the most recent technological leap in time keeping. There are a few different types but all rely on atomic transitions, which are a fundamental property of the atoms and do not vary in time or due to environmental conditions. These atomic transitions appear due to energy levels in the atoms, and from the Planck relation $E = hf$ can be driven by a frequency. A local oscillator, often quartz [19], can drive this transition, with the absorption of this signal being measured. If frequency drifts the absorption will drop; if this drop is used to feedback to the

oscillator then it will stabilise itself in a feedback loop, and this stable frequency can then be used to produce a pulse-per-second output giving a time measurement. The first atomic clock was developed by the National Bureau of Standards in 1949 using transitions in an ammonia molecule [20]. The most accurate atomic clocks currently are optical, operating at higher frequencies than previous types and have stability on the order of 10^{-18} [21], taking approximately the age of the universe to lose 1s [22]. Atomic clocks are so stable that we now define the length of a second using a transition frequency of caesium measured in an atomic clock [23].

1.2 Global Navigation Satellite Systems

One of the key applications of atomic clocks is in global navigation satellite systems (GNSS) e.g. the global positioning system (GPS). These work by triangulating the receiver position by timing the transfer of microwave signals from satellites. These satellites each have synchronised atomic clocks at time t_s. The microwave signals carry information but these take time to arrive. This can be used to calculate the distance to the receiver using:

$$t_r - t_s = \frac{D}{c} \tag{1.1}$$

where t_r is the time on the receiver clock, D is distance between receiver and satellite and c is the speed of light. On its own this isn't enough to narrow down a position as any point on a sphere of radius D are potential positions. However with multiple satellite a position can be found by taking only positions where the spheres overlap. Unfortunately due to uncertainties this position will have an area, as each sphere is actually a shell of non-zero volume.

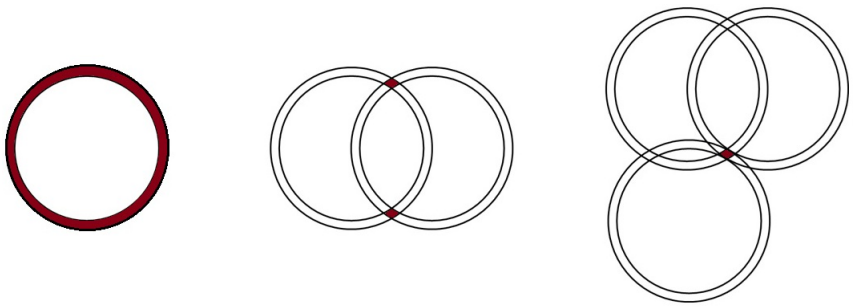

Figure 1.1: Simplified diagram of how triangulation can be used to narrow down an area (possible positions shown in red).

One of the main sources of uncertainty is in the synchronisation of the two clocks, if the receiver clock drifts then the uncertainty in location increases, meaning that a more stable receiver clock increases the resolution of the GNSS. This is

particularly beneficial when fewer satellites are available as less triangulation means the uncertainty in t_r has a greater effect. If the receiver time is well known then only 3 satellites should be needed to determine accurate location information. Of particular interest to military applications is an increase in resistance to GNSS jamming. Jamming often works by blocking part of the microwave signal [24]. Larger deviations require a wider search of the signal sequence which is problematic if part of it is blocked; this makes more stable clocks more resistant to jamming, and due to the smaller search, they are also able to reacquire the signal faster. Furthermore a more stable clock also needs to be reacquired less often further increasing resistance to jamming.

1.3 Chip Scale Atomic Clocks

Having miniaturised atomic clocks small enough to be used as the receiver clock would clearly lead to a big improvement in GNSS accuracy. The ideal would be a chip scale atomic clock (CSAC). These don't aim to be more accurate than the best atomic clocks but offer much greater potential for miniaturisation. There are a few different types of CSAC but they most commonly operate using coherent population trapping (CPT) [25]. Optical and microwave sources are tuned to the transition frequencies of alkali atoms, most commonly ^{133}Cs or ^{87}Rb [25]. Alkali atoms are used due to their single valence electrons, giving a comparatively simpler structure. Two ground states are simultaneously excited by a single laser source which is modulated at half the hyperfine frequency. This causes destructive interference, pumping the system into a dark state, increasing the optical transmission. This is then detected and error corrected. Importantly, as the microwaves are applied directly to the atoms in the form of the modulation of the laser current there is no need for a microwave cavity, simplifying and shrinking the required equipment [26]. Shown below are examples of current CSACs and their key specifications:

Company	Product Title	Allan dev. (1s)	Size (cm^3)	Weight (kg)	Power (W)
Microsemi	SA45.s	3×10^{-10}	17	0.035	0.12
Teledyne	TCSAC	3×10^{-10}	23	0.042	0.18
Chengdu Spaceon	CPT	2×10^{-10}	24	0.045	1.6
Accubeat	NAC	2×10^{-10}	32	0.075	1.2
Spectratime	mRO-50 (EAS)	4×10^{-11}	50	0.075	0.036

Table 1.2: Specifications for a selection of commercially available chip scale atomic clocks, reproduced using data from [26]

In this table the Allan deviation (Allan dev.) is a measure of the clock stability (explained further in section 2.0.2). In this case the stability over one second, this time frame is chosen as it allows longer term fluctuations, like those in temperature and magnetic field, to be neglected.

1.4 The Endohedral Fullerene $^{15}N@C_{60}$

The clock in development at Lancaster University uses the transitions of the endohedral fullerene $^{15}N@C_{60}$. This is a nitrogen-15 atom inside a carbon cage. It is important to justify the use of this material considering its extremely high cost, being one of the most expensive materials in existence at £200,000,000 per gram [27]. This extremely high cost is due to the difficulty in manufacturing. Firstly ^{15}N accounts for only a very small proportion of nitrogen, less than 0.4% [28]. These nitrogen ions are accelerated onto a film of C_{60} by an ion beam however most of them pass through without implantation or shatter the fullerene cage. Because of this continuous running doesn't make sense considering the rarity of ^{15}N so it is run for only a few hours and then refined with multiple runs of high pressure liquid chromatography [27]. Even with the high cost and difficulty in manufacturing, it is still worth using due to several factors. Firstly, it has a narrow linewidth, estimated to be $\delta \sim 100$kHz at the clock transition[29]. This is needed as a sharper transition will result in a larger difference if the input frequency drifts at all, making corrections easier and reducing Allan deviation (explained further in section 2.0.2). $^{15}N@C_{60}$ has many transitions but importantly has one 'clock transition'. This is a transition where under small changes in magnetic field the transition frequency is invariant and can be seen as the minimum on the parallel section of Figure 2.1. When trying to build a stable clock this is obviously extremely useful, making the clock more stable, particularly in the presence of varying magnetic fields.

Other than accuracy the key properties for a CSAC are size weight and power (SWaP). For certain applications the increased accuracy that a CSAC can provide over a quartz oscillator is worth the increased SWaP, however the more SWaP requirements can be minimised the wider the spread of applications, in the long term potentially replacing quartz oscillators in consumer electronics. Vapour chambers like those used in CPT CSACs are hard to miniaturise, large, heavy and power hungry. A clock using $^{15}N@C_{60}$ has no need for a vapour chamber, offering a simpler design, and greater potential for reducing SWaP. Furthermore the lower transition frequency allows for more off the shelf RF components to be used, simplifying development and reducing costs. Additionally $^{15}N@C_{60}$ can also be measured at room temperature, another clear benefit for SWaP. Finally the fact that the sample can be dissolved into solution is useful particularly due to the high solubility limit in

CS_2 (the solvent used). This allows for a high spin density leading to a larger voltage response improving the signal-to-noise (S/N) ratio. With all this being said a clock using $^{15}N@C_{60}$ will almost certainly never compete against leading atomic clocks in terms of accuracy, however the benefits in SWaP make it a potential alternative for CSACs.

A potential clock would work on the principle of frequency feedback. A constant magnetic field creates a transition in the sample and then a signal is sent to the sample at the corresponding frequency. The absorption of this signal is measured by monitoring the reflected signal. If the input signal's frequency drifts the absorption will drop as it is no longer on resonance. This change is monitored and a corresponding change is made in the oscillator to return to resonance. This is called frequency feedback. This helps explain some of the choices made in design as sharp transitions are needed, making smaller drifts measurable and frequency feedback more sensitive.

As of yet the best measurement of Allan deviation measured in the group's clock is worse than both conventional quartz clocks and other CSACs [29], however the clock is still in the process of optimisation. The theoretical limit of its Allan deviation is not yet known, but an estimation of this can be made. To find this estimation the intrinsic linewidth at the clock transition must be found, and as of yet this has not been successfully measured. The linewidth can be calculated using the T_2 relaxation time, which can only be measured using pulsed electron paramagnetic resonance (EPR) due to linewidth broadening effect present in the more conventional continious wave (CW) EPR. This is explained further in section 2.0.3. The specific transition of interest is a 'clock transition' which occurs at 38.6MHz in parallel mode. Currently the closest successful EPR measurement to this is at 102MHz in perpendicular mode [30]. Therefore the overall aim of this project is to use pulsed EPR to take a measurement at a lower frequency and investigate parallel mode operation.

Chapter 2

Theory

There are two types of electron paramagnetic resonance (EPR): continuous wave (CW) and pulsed. We will first examine CW EPR; this is the simpler type, so serves as a useful introduction to EPR, and is also the type currently used by the Lancaster research group's clock and the type they plan to use in their CSAC. The fundamental way this works is by sending a radio frequency (RF) signal to a resonator. This causes a magnetic field to be induced at the resonant frequency of the resonator. If the frequency matches a transition energy of the sample this energy is absorbed. This is recorded by measuring the reflection back from the resonator. The transitions are dependent on a static magnetic field (B_0) created by Helmholtz coils, which is varied depending on the sample under investigation ($^{15}N@C_{60}$) as well as the orientation of $\vec{B_0}$. The two other samples used in the investigation were 2,2-diphenyl-1-picrylhydrazyl (DPPH) and lithium phthalocyanine (LiPc). These samples were each used in preliminary experiments to troubleshoot due to their much larger magnitude EPR signals. DPPH was used for CW and LiPc was used for pulsed EPR.

This is conventionally done in one of two ways, varying either frequency or magnetic field to produce a line spectrum. For the purpose of this project the magnetic field was scanned across transitions to identify and measure their respective amplitudes.

2.0.1 Zeeman Effect And Transition Energies

EPR uses electron spin resonances and the Zeeman effect to create transitions. When a magnetic field is applied to single electrons a torque is applied on the spins which are neither aligned nor anti-aligned with the field, causing spins to become aligned in one of those two states. These have an energy difference between them, proportional to the strength of field applied. This allows for specific energy differences and

therefore frequencies to be investigated by selecting the corresponding magnetic field. For this to be the case we need to quantify these transitions.

To understand these we first need to understand Larmor precession. This is the characterization of the torque, $\boldsymbol{\tau}$ applied by the magnetic field on the spin magnetic dipole. This results in a change in angular velocity. The frequency of precession for the spin magnetic dipole, $\boldsymbol{\mu}$ around the direction of the magnetic field is given by:

$$\omega = \gamma B \tag{2.1}$$

where ω is the Larmor frequency and γ is the gyromagnetic ratio. When the magnetic field is alternating at this frequency a resonance occurs and energy can be absorbed.

This energy can be quantified by looking at the energy difference between the two spin states. Electrons have a spin value of 1/2, and therefore have spin magnetic numbers of $m_j = \pm 1/2$. For a single electron the energy of each state in a magnetic field is given by:

$$E = m_j g_e \mu_0 B_0 \tag{2.2}$$

where g_e is the Landé g factor, μ_B is the Bohr magneton and B_0 is the magnetic field strength. As $m_j = \pm 1/2$ the energy difference between these two states is:

$$\Delta E = g_e \mu_B B_o \tag{2.3}$$

From the Planck relation $E = hf$ this gives a frequency required to drive the transition of:

$$f = \frac{g_e \mu_B B_0}{h} \tag{2.4}$$

This energy is supplied by the oscillating magnetic field produced by the resonator, and due to quantisation this frequency must be exact. While useful to understand, this is for a free electron; the picture is more complicated for an unpaired bound electron like that in $^{15}N@C_{60}$. There are several more interactions which need to be considered.

The first is spin orbit coupling. This is the interaction of spin and orbital angular momentum, leading to the fine structure of energy levels in the atom. Due to symmetries in $^{15}N@C_{60}$ the electron's angular momentum is 0 meaning that this can be ignored. Secondly, we need to consider the hyperfine structure of the atom. This is caused by two effects: the Fermi contact interaction, an overlap of electron and nuclear wave functions; and magnetic dipole coupling, which is the interaction between the dipoles of the electron and the nucleus. These cannot be ignored. We must also consider zero field splitting; this is caused by electron spins coupling to each other, occurring when there are more than one unpaired electron i.e. when

the quantum spin number $S \geq 1$ [31]. Although $S = 3/2$ for ^{15}N, due to the fullerene's high number of symmetries there is minimal interaction so this can also be ignored. The last factor to consider is quadrupolar coupling, which is the coupling of the nucleus' magnetic and electric fields; occurring when nuclear spin magnitude I >1/2. This is only true of nuclei with non spherical charge distributions so can be ignored for $^{15}N@C_{60}$ [32].

These considerations give the following Hamiltonian for $^{15}N@C_{60}$:

$$\hat{\mathcal{H}} = g_j \mu_B B_0 \hat{S}_z - g_N \mu_N B_0 \hat{I}_Z + A\vec{S} \cdot \vec{I} \tag{2.5}$$

Due to the high amount of symmetry in $^{15}N@C_{60}$ all the spins experience the same conditions even though there are various configurations of quantum numbers, meaning that in this case g_j and A are both scalars.

This Hamiltonian can be used to create plot of the transition energies against magnetic field. These were done by Harding et al. [29]. This is shown below:

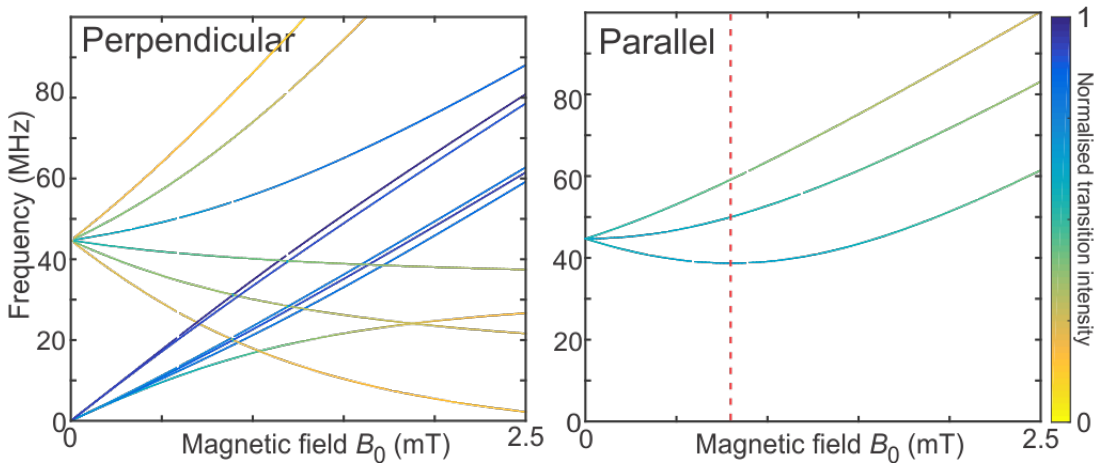

Figure 2.1: Simulated EPR transitions coloured according to transition intensity in perpendicular mode (left) and parallel mode (right). The clock transition is marked with the dashed line. Produced by Harding et al. [29]

Perpendicular and parallel mode refer to the orientation of the two magnetic fields, the primary magnetic field B_0 which creates the energy difference due to the Zeeman effect, and the modulating magnetic field, B_1 which drives the transition between the two states. As stated in the introduction the most important transition here is the minimum seen in parallel mode at 38.6MHz; this is invariant to small changes in magnetic field making a potential clock more stable. In this project transitions at various frequencies were investigated, usually chosen for transition intensity or

producibility of magnetic field at resonator frequency; the Helmholtz coils are limited in their range of producible magnetic fields by heat constraints.

2.0.2 Allan Deviation

The Allan deviation is a measure of the stability and therefore quality of a clock, specifically the stability of its oscillator, telling us how the frequency of the oscillator varies over time. To characterise the stability, we first need to find the frequency difference at all points from the resonant frequency, producing the instantaneous normalised frequency difference:

$$y(t) = \frac{\omega(t) - \omega_0}{\omega_0} = \frac{\Delta\omega}{\omega} \tag{2.6}$$

where $\omega(t)$ is the instantaneous frequency at time, t and ω_0 is the resonant frequency. This is a continuous function; to find discrete values this is integrated over a time τ and normalised to find the average value:

$$\bar{y}_i = \frac{1}{\tau}\int_{t_i}^{t_i+\tau} y(t)dt \tag{2.7}$$

These averages are clustered into groups of length τ to be compared against the mean; each cluster is consecutive [33]. The mean is found by:

$$\bar{y} = \frac{1}{N}\sum_{i=1}^{N} y_i \tag{2.8}$$

Traditionally the variance is the difference between the average of each cluster and the mean:

$$\sigma^2 = \frac{1}{N-1}\sum_{i=1}^{N}(y_i - \bar{y})^2$$

Unfortunately for a clock this would only ever diverge making it not very useful for parametrising their stability, instead the Allan variance is used, this instead measures the difference between the average values of adjacent clusters [34], therefore measuring how the frequency of the clock varies over time. This is found using:

$$\sigma_y^2(\tau) = \left\langle \sum_{i=1}^{2}(\bar{y}_i - \frac{1}{2}\sum_{j=1}^{2}\bar{y}_j)^2 \right\rangle = \frac{1}{2}\left\langle(\bar{y}_2 - \bar{y}_1)^2\right\rangle \tag{2.9}$$

where $< ... >$ is the expectation value. Finally the Allan deviation is simply:

$$\sigma_y(\tau) = \sqrt{\frac{1}{2}\left\langle(\bar{y}_{i+1} - \bar{y}_i)^2\right\rangle} \tag{2.10}$$

This is the definition of the Allan deviation and can be measured in a clock, however the pulsed EPR set up used in this project cannot be used to find this.

Instead an estimate of the Allan deviation can be made based off the measured linewidth. The standard deviation in a signal V is related to variations in the driving frequency, ω, through the gradient on resonance.

$$\sigma_\omega = \sigma_V \frac{\delta\omega}{\delta V} \tag{2.11}$$

When on resonance this gradient can be approximated to be linear, so can be found using the full width at half maximum, $d\omega$ and the half the peak amplitude, $\frac{1}{2}V_{max}$:

$$\frac{dV}{d\omega} = \frac{\frac{1}{2}V_{max}}{\frac{1}{2}d\omega} \tag{2.12}$$

Furthermore the variation in V, σ_V is a measure of the noise in V, so we can convert into a S/N ratio:

$$\frac{\sigma_V}{V_{max}} = \frac{1}{\text{S/N}} \tag{2.13}$$

Combining these two equations into 2.11 gives the variation in ω:

$$\sigma_\omega = \frac{d\omega}{\text{S/N}} \tag{2.14}$$

Assuming that the variation is due to white noise, the standard deviation over a measurement time τ is scaled by:

$$\sigma_V(\tau) = \sigma_V(\tau = 1s)\frac{1}{\sqrt{\tau}} \tag{2.15}$$

This is only true in this case for short time frames, i.e. over 1s, for longer time frames the variation cannot be assumed to be white noise due to longer term drifts. Finally the Allan deviation is the normalised frequency deviation over a time τ which is given by:

$$\sigma_y(\tau) \equiv \frac{\sigma_\omega}{\omega_0} = \frac{\delta\omega}{\text{S/N} \times \omega_0} = \frac{1}{\text{S/N}}\frac{1}{Q}\frac{1}{\sqrt{\tau}} \tag{2.16}$$

where Q is the quality factor [35, 30]. The quality factor is defined mathematically in equation 2.18, and is a measure of the sharpness and duration of the resonance. Importantly the frequency linewidth, $\delta\omega$, the S/N ratio, the resonant frequency ω_0 and the Q factor are all able to be found for a given EPR measurement. This can only be used over short time frames, e.g. 1s, assuming that the noise of the system is purely white noise. This is the origin of the factor of $\frac{1}{\sqrt{\tau}}$, over longer durations

other deviations like those caused by drifts in magnetic field strength or temperature fluctuations would need to be taken into account.

For this to be measured a T_2 relaxation time must be found, as this can be used to calculate the frequency linewidth using:

$$\delta\omega = \frac{1}{\pi T_2} \tag{2.17}$$

This T_2 time is the transverse spin relaxation time, which is the time taken for the spin signal to reduce by a factor of $\frac{1}{e}$. This is caused by spin-spin relaxation and magnetic field inhomogeneity [36].

The Q factor is also required; this is given by:

$$Q = \frac{\omega_0}{\delta\omega} \tag{2.18}$$

Using this an estimation of the short term Allan deviation can be found from data gathered using pulsed EPR.

2.0.3 Pulsed Theory

From equation 2.17 the T_2 must be measured to find the intrinsic linewidth, which can then be used to estimate the Allan deviation, however this relaxation time cannot be measured using CW EPR due to various linewidth broadening effects. Firstly there is a broadening due to the modulation field B_{mod}. This is required in CW to a certain extent as a smaller modulation amplitude leads to a smaller EPR signal, worsening the S/N ratio [37], [38]. Some level of field inhomogeneity must exist for a sample with a volume, this effect is minimised by using Helmholtz coils which produce a very homogenous field but this does not completely remove this effect. This causes the spins in the sample to see varying degrees of magnetic field, further causing broadening [39]. Finally power broadening also increases the linewidth. The signal intensity depends on the population difference in the two spin states, however if the input power is too high then this will saturate, weakening and broadening the signal [40] [41]. This can be optimised, however some broadening is unavoidable.

Pulsed EPR can avoid these intrinsic broadening effects, allowing for T_2 to be measured. Rather than a continuous signal constantly transmitting energy to the sample as per CW, pulsed EPR sends short bursts of signal causing excitation and then relaxation of spins. Various pulse sequences can be used depending on the goal of the investigation. The simplest of these and the one used in the project is Hahn echo. This uses the following sequence:

$$\frac{\pi}{2} \rightarrow \tau \rightarrow \pi \rightarrow \tau \rightarrow \text{echo}$$

The $\frac{\pi}{2}$ and π are the angles of rotation applied to the spins of the sample. Initially the spins are aligned by the magnetic field, and a $\frac{\pi}{2}$ pulse is applied. For example with an orientation of +z, this then rotates the magnetisation into +x. The spins in the sample begin to relax in the xy plane, away from the +x, however they do not all relax in the same direction or with the same speed. The result is a fanning out of the spin magnetisation vectors [42]. After a time, τ the π pulse then rotates the spins in such a way that their positions are flipped on the xy plane. As the spins retain their momentum the previous spreading of spins now causes them to realign after a time τ now aligned with -x. This realignment produces a measurable voltage and is seen as an echo. A simplified model of this is shown in figure 2.2.

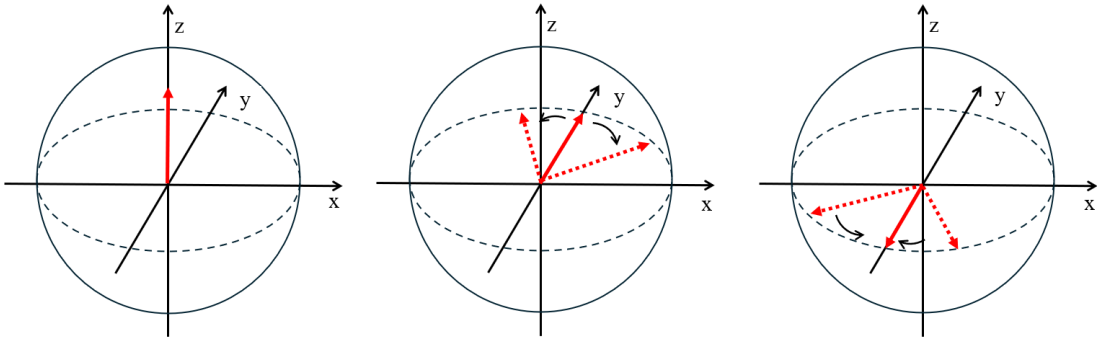

Figure 2.2: Bloch sphere representation of a Hahn echo sequence: (left) the spin magnetisation vector is initially aligned in z due to the constant magnetic field B_0; (centre) the spin magnetisation vector after the $\frac{\pi}{2}$ pulse applied, which is then given time, τ to relax on the xy plane; (right) the spin magnetisation vector after the π pulse and a second relaxation time, τ, after which realignment occurs due to conservation of momentum.

This model shows only the affect of the pulses on the spin magnetisation with the in-plane relaxation. This demonstrates why an echo is measured after a delay of τ seconds after the second pulse. This does not show either the affect of the constant magnetic field, B_0 or the longitudinal spin relaxation. The constant magnetic field would apply a torque to the spins causing them to rotate in-plane, and the longitudinal relaxation is caused by spin-lattice relaxation, where the spins relax from the excited state caused by the pulse back to their original state, in this case aligned with z. The combination of these would be the spins spiralling upwards. This is in addition to the pulses and was excluded from the diagram for clarity.

For this to work the input signal's power and duration must be optimised to cause the correct amount of rotation. The separation time, τ can be selected. A larger separation time reduces the magnitude of the echo. This is because there is more time for spin-lattice relaxation to occur, where the nuclear magnetic moment of the

spins re-aligns with the constant magnetic field B_0, in this case towards +z. Overall this causes a reduction in the total magnetisation of the spins on the xy plane reducing the magnitude of the echo. The magnitude of the voltage is characterised by:

$$V = V_0 e^{-\frac{2\tau}{T_2}} \tag{2.19}$$

where V is the voltage produced; V_0 is the maximum theoretical echo voltage given no spin-lattice relaxation, so when $\tau = 0$; as before τ is the separation time; and T_2 is the spin relaxation time which can be found by fitting this equation to a series of Hahn echo results.

Phase cycling can be added to this to increase S/N ratio. This is the process of alternating the phase of the pulses causing alternating rotations in spins. For example following a pulse of +x, causing the magnetisation to rotate to -y, with a pulse of -x, which then causes a rotation to +y. Each of these produces a voltage trace; the second is subtracted from the first. As the magnetisation is opposite, so is the voltage; this subtraction will therefore roughly double the seen signal. Importantly this also reduces noise; noise from switching and ring-down of the resonator are both reduced by this as their signals are not flipped, so the subtracting should cancel these out. This does not entirely remove this noise however a large reduction is seen. This is two-step phase cycling, however in this project four-step phase cycling was used. The next steps in the sequence are in ±y; these effectively flip the inputs of the two digitiser channels. This increases the noise-reduction effect of the two-step cycle, and also removes any imbalance between the two chains up to the channels.

Chapter 3

Methodology

3.1 CW EPR

CW EPR was investigated mainly to gain experience with the equipment and code base. This was very useful as pulsed EPR is more complex, but operates with similar equipment and code. The aim was to simply take successful CW EPR measurements, particularly of $^{15}N@C_{60}$. The set up operates on the principles of radio frequency

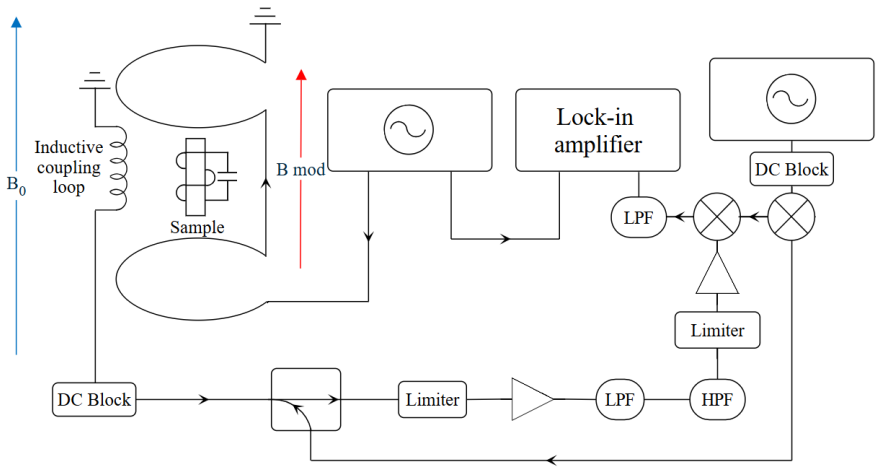

Figure 3.1: Complete circuit diagram of the continuous wave EPR spectrometer. The signal is produced at the desired frequency by the signal generator, and directed to the sample. The absorption is measured using the reflected signal, which is amplified, filtered (LPF and HPF are low and high pass filters respectively) and then mixed with the original frequency. The modulation coils create an oscillating magnetic field which the lock-in amplifier uses to demodulate the output at the frequency of this modulation.

(RF) reflectometry. A signal is sent to the sample and a measurement of the reflected signal is made. The constant magnetic field B_0 produced by the Helmholtz coils creates the energy difference in the sample. This is due to the Zeeman effect (as per section 2.0.1). The sample used in the investigation was made with a 1.5mg mixture of C_{60} and $N@C_{60}$, with a concentration of 22000ppm of $N@C_{60}$. This was dissolved in CS_2 at approximately the solubility limit of 7.9mg/ml. In total the number of spins was N $\approx 2.76 \times 10^{16}$.

These encompass an aluminium box with the sample inside. The box provides shielding from AC noise. Modulation coils provide the varying magnetic field which is needed for phase-sensitive detection . These are too close to act as Helmholtz coils, reducing the field homogeneity, however this increases the produced field strength which is required in this case. These are driven by a waveform generator at 6kHz. The signal to the sample is produced by an RF generator and, through the resonator, drives the transitions within the sample. The signal is sent through a DC block to minimise reflections and then split, one goes to a directional coupler and thus to the coupling loop, the other is used in the later mixing process.

The coupling loop is a single loop of wire connected to a platform. This platform can be raised and lowered using a differential screw to optimise coupling to resonator, and can be seen on figure 3.3. The resonator is inductively coupled to the coupling loop with the aim for it to be critically coupled, where the impedance of the resonator matches the impedance of the coupling loop. The resonator, due to the alternating current induced from the coupling loop, produces the alternating magnetic field, B_1, which provides the energy to induce transitions within the sample. The coupling is measured by a network analyser (NA), this is not shown in the circuit diagram, figure 3.1, as it is not present while a measurement is being carried out; the coupling is optimised before starting a measurement. The NA plugs directly into a coaxial line going to the coupling loop.

While coupling the NA continuously transmits through the coupling loop. This allows for the level of coupling to be seen in real time as adjustments are made using the differential screw. A screw is used as it easy to adjust while still being able to produce very small changes in platform height, meaning that the coupling can be precisely controlled, and once the desired level has been achieved the screw holds the platform in place. The NA is now used to take a measurement of the Q factor and the precise resonant frequency of the resonator. This is done by measuring the transmission of a signal through the coupling loop; on resonance a large drop in transmission is seen. The exact location of the resonance is found using the full width at half maximum. The point halfway along the width gives the exact resonant frequency. Two examples of this are shown in figure 3.2.

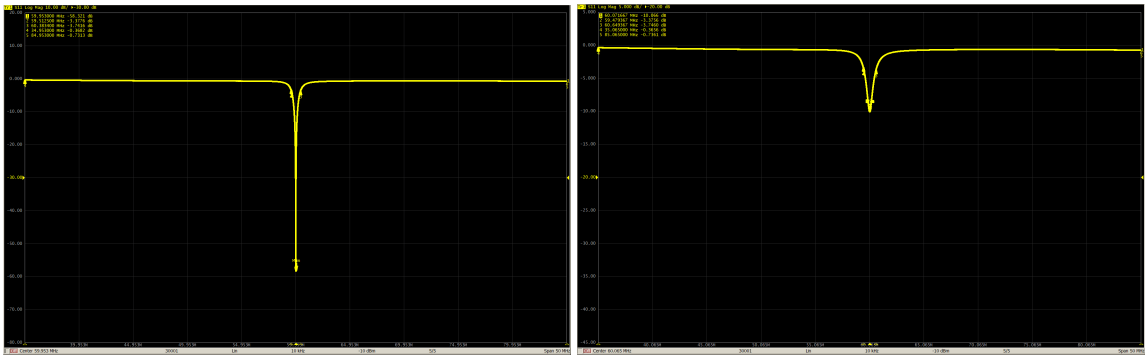

Figure 3.2: Network Analyser frequency scans of a Loop Gap Resonator, critical coupling (Top), over-coupled (Bottom)

When on resonance the magnetic susceptibility of the sample modifies the impedance of the resonator causing it to no longer be impedance matched. The magnetic susceptibility is a measure of how much the sample is magnetised in an external magnetic field. As the sample is magnetised it alters the magnetic field, and thus the flux through the resonator, changing its inductance; as the impedance of an LC circuit is directly proportional to its inductance this is also changed. This causes a portion of the signal to be reflected back to the coupling loop through the circuit. The reflection passes through the directional coupler and through a chain of amplifiers and filters. Limiters are included to prevent potential damage to the amplifiers, which have a total of 46dB of gain. The filters are a low pass filter (LPF) and a high pass filter (HPF) with a bandpass of 27.5-48MHz, which reduce noise. The signal is then mixed in a homodyne arrangement: the original signal which was split off is mixed with the spin modified signal. The output is a signal at the modulation frequency (6kHz), which then passes through another LPF of 10kHz before entering the lock-in amplifier.

Lock-in amplifiers use phase-sensitive detection to amplify a signal at a specific frequency. A phase-sensitive detector (PSD) multiplies the signal by a reference signal. For a general signal of form $V\sin(\omega t+\theta)$, where V is signal amplitude, ω is the signal frequency and θ is the signal phase, this multiplication gives:

$$V_{PSD} = V_{sig}V_{ref}\sin(\omega_{sig}t+\theta_{sig})\sin(\omega_{ref}t+\theta_{ref}) \tag{3.1}$$

This equals:

$$V_{psd} = \frac{1}{2}V_{sig}V_{ref}\cos([\omega_0-\omega_{ref}]t+\theta_{sig}-\theta_{ref}) - \frac{1}{2}V_{sig}V_{ref}\cos([\omega_0+\omega_{ref}]t+\theta_{sig}+\theta_{ref}) \tag{3.2}$$

As this is an AC signal, it will be removed by the low pass filters present, unless the two frequencies, ω_0 and ω_{ref} are equal, resulting in a DC signal, proportional to the V_{sig}:

$$V_{psd} = \frac{1}{2} V_{sig} V_{ref} cos(\theta_{sig} - \theta_{ref}) \tag{3.3}$$

This output clearly depends on the phase of the two signals. This can be eliminated with a second PSD. This multiplies the input signal by the reference signal phase shifted by 90°. These are done separately, producing two outputs. The sum of these in quadrature gives the magnitude of the signal and has no phase dependency [43]. However this can make optimising the output voltage using the phase of the system difficult; in our case both outputs are measured and the phase is selected so that one output is maximised. The experiment is controlled using Python scripts; the drivers for instruments are all written in Q codes apart from for the lock-in amplifier which uses a proprietary driver from Zurich Instruments.

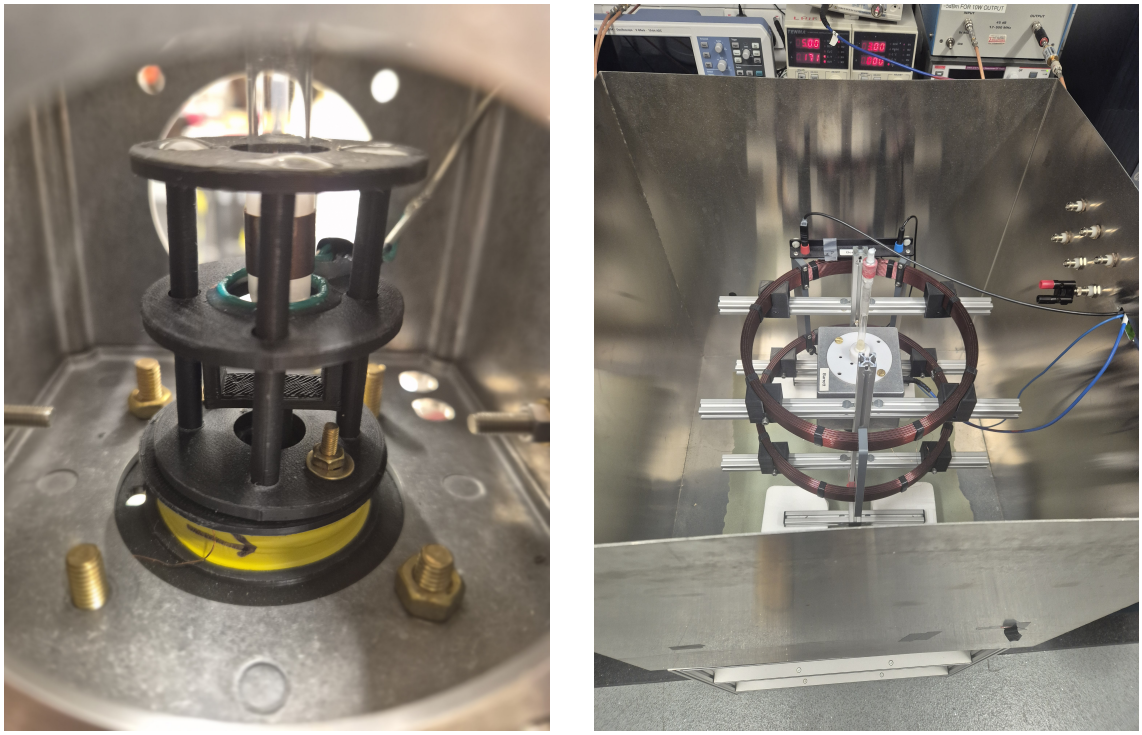

Figure 3.3: Interior of the spectrometer. The coupling loop is seen in green, on the platform which can be raised and lowered; lower modulation coil can also be seen in yellow (left). Full spectrometer, seen in parallel mode (right).

Finally in figure 3.3 on the right a magnetic shielding box can be seen. This was not used in CW, and was a late addition for pulsed EPR to try to improve the S/N ratio. No major difference was observed after its addition, however it should provide some magnetic shielding, this is likely not a large amount due to the shield being partially

saturated by the field produced by the Helmholtz coils which is much larger than the background field.

3.2 Pulsed EPR

As stated in the section 2.0.3 continuous wave EPR cannot find the T_2 relaxation time that would allow for an estimation of the Allan deviation due to linewidth broadening effects. Because of this pulsed EPR must be used. This section explains the setup and method used to investigate pulsed EPR and find the T_2 time. The spectrometer itself is unchanged between CW and pulsed, staying as pictured in figure 3.3. The full circuit diagram is shown below:

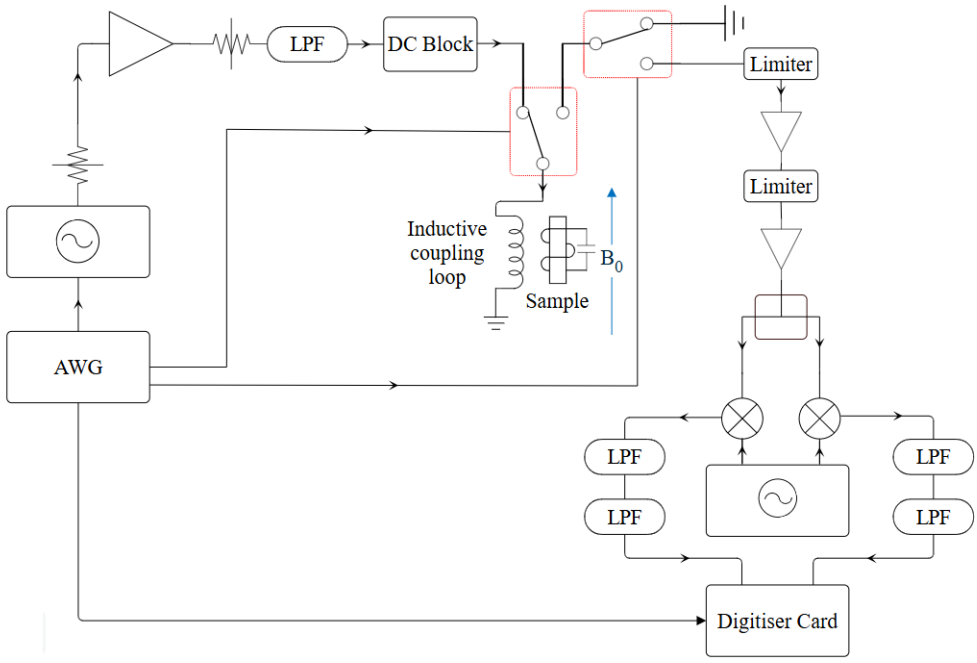

Figure 3.4: Complete circuit of the pulsed EPR spectrometer. Pulses are produced by the arbitrary waveform generator, and are IQ modulated before being sent to sample. These cause excitation, relaxation and finally realignment. This is measured as a voltage produced in the coupling loop. Mixing is used to convert the signal into a DC voltage which can be measured at digitiser card.

The equipment is primarily run by an arbitrary waveform generator (AWG). Firstly π and $\frac{\pi}{2}$ pulses are produced (shown in Figure 3.5), these control the signal outputted by the signal generator using IQ modulation. This is amplified to the desired power, filtered and partially attenuated to minimise noise, and then sent to the sample.

This is timed alongside a signal also produced by the AWG and sent to the switches.

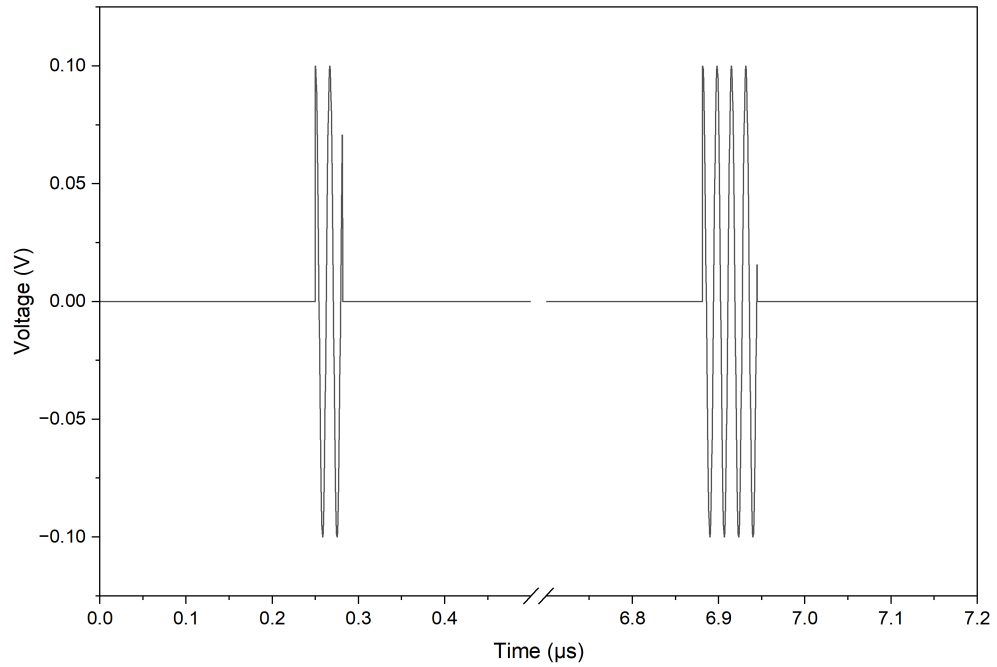

Figure 3.5: Visual representation of the $\frac{\pi}{2}$ and π pulses sent to the sample, with 6.5μs Hahn separation and 100ns π duration

The first of these is the directing switch: this allows the signal to be sent to the sample and then switches to the measurement chain to allow for detection. It is important to use a switch rather than a directional coupler (as used in CW) due to the presence of ring-down. The ring-down of the resonator is inherent to pulsing as there is time between pulses for the resonator to relax. This occurs over a short time frame so that most of the ring-down can be sent back along chain to the signal generator rather than towards measurement chain. To have this time frame be short the resonator must be over coupled. The ring-down time follows $e^{-\frac{\omega t}{2Q}}$, meaning a reduction in Q factor increases the rate at which the ring-down occurs. This is why the resonator is over coupled, as this reduces the Q factor. This reduction reduces the amount of power sent to the sample due to the impedance mismatch causing more reflection (explained further in 4.1), but is required as the ring-down can completely obscure the echo. The switching also protects the amplifiers which can be saturated by the ring-down. This switch is a high power switch capable of withstanding the high power pulses but it also has a high amount of video noise [30]. Similarly to the ring-down this can also obscure the echo. Because of this a second switch is used: the shielding switch. While the switching of the directing switch takes place, the shielding switch faces a terminator, only facing the measurement

arm once this has finished. This switch has the added benefit of further reducing the ring-down seen by the measurement chain.

The signal is then sent along the measurement chain to be amplified; as in the CW case limiters are present before each amplifier to protect them from saturation and potential damage. Similarly to in the CW case the signal is then mixed, however unlike in CW a lock-in amplifier cannot be used. This is due to the time dependence of the signal in pulsed EPR; the iterative filtering process in a lock-in amplifier distorts the echo, flattening and broadening it. However the set up of mixers and filters in 3.4 effectively acts in the same way: using homodyne mixing, multiplying the signal by a reference frequency, in this case the same as the drive frequency. Due to the low pass filters this again only produces an output when the reference frequency and drive frequency are equal, as in equation 3.3 producing a DC output. Similarly to a lock-in amplifier the signal is split and multiplied by two reference signals, one of which is phase shifted by 90° so that both the in phase and quadrature components can be measured. The LPFs used are Bessel filters, due to their constant group delay [44]. This applies an equal delay to all frequencies, retaining the shape of the echo. This output is then sent to the digitiser card which acts as a DC voltmeter and records the two inputs which are stored before averaging and smoothing is carried out. The card is also triggered by the AWG.

Similarly to CW this can be set up in perpendicular and parallel mode. This is determined by the orientation of the Helmholtz coils and therefore of B_0 with respect to the resonator field, B_1. Both perpendicular and parallel mode measurements were taken. A scan involves measuring over a range of discrete magnetic fields, with multiple measurements being done at each field value to then average over, increasing the S/N ratio. Part of this averaging is adding phase cycling, as described in 2.0.3.

3.2.1 Parallel Mode Operation

For parallel mode operation the only change the in set up is a rotation of the Helmholtz coils to be parallel to the resonator field. As per figure 2.1 this results in a change in transitions. As stated earlier the 'clock transition' (38.5MHz) is invariant to small changes in magnetic field. For this to be measured first a higher frequency measurement in parallel mode should be made, as signal intensity reduces with frequency. It is also worth noting that the expected signal in parallel mode is weaker than in perpendicular mode, requiring a comparatively better signal-to-noise ratio (S/N). This is due to the different Hamiltonian for parallel transitions.

Because of this difference different parameters were used and investigated. Pulse separation can be optimised for, however to produce the estimation of Allan deviation this needs to be varied. This leaves pulse duration as the most important

variable to optimise. This was optimised in perpendicular mode but is expected to be slightly different in parallel, again due to the different Hamiltonian. Therefore a series of measurements with varying pulse durations was carried out. This is controlled by a parameter in the Python script, so was varied and scanned.

Many difficulties were encountered in parallel mode. Because of these extensive investigations were carried out. Firstly, individual circuit components were checked by measuring the transfer of a signal through the component with a NA and comparing it to the expected result. All components acted as expected. The echo signal was still not visible so a more thorough investigation into the S/N ratio of the circuit was carried out; more details on this are in sections 5.2.3 and 5.2.5.

Chapter 4

Optimising the electrical resonator

4.1 Resonator Theory

There are two types of resonator in use in this project. The first are loop gap resonators (LGRs); these are a hollow cylinder of copper with a small section cut from the circumference where capacitors are soldered across. The other is a solenoid resonator, a coil of copper wire whose free ends are connected with capacitors. Both of these designs were developed before my arrival on the project. These resonators create the magnetic field which excites the sample and are coupled to the circuit using the inductive coupling loop. The solenoid resonators have considerably higher Q factors for a given frequency; this is very useful in continuous wave EPR, but too high to be used in pulsed EPR due to ring-down, so LGRs are still used there. Both of these have lower Q factors than the more conventional resonators used in EPR (tuneable microwave cavities) however are more appropriate in this use case for several reasons: they are more practical due to their smaller size [45], they exhibit reduced difference in Q factors at lower frequencies and offer higher filling factors for small sample volumes [46], [47]. While the current resonators are functional, improvements can still be had, a higher Q factor would increase the S/N ratio in CW EPR, and they are currently very fiddly to make, particularly making them consistently at the exact same frequency. Three new techniques to create solenoid resonators were tested with this in mind. It is first useful to understand the properties which govern the behaviour of resonators. The resonant frequency, f depends on the physical properties of the resonator, namely the inductance, L and the capacitance C. This relation is given by the following equation:

$$f \approx \frac{1}{2\pi\sqrt{LC}} \tag{4.1}$$


Figure 4.1: An LGR (left) and a solenoid resonator (right)

Using this the specific frequency desired can be chosen. For both the LGR and solenoid the internal capacitance is negligible compared to the capacitance of the added capacitors, so the overall capacitance can be approximated as the capacitors' capacitance. The capacitance is more often varied to get the desired frequency as it is easier to switch by adding, removing or switching to a different value capacitor rather than changing the main body of the resonator. The properties of the body are what dictate the inductance, which is given by:

$$L = \frac{N^2 \mu_0 \pi r^2}{l} \tag{4.2}$$

where N is number of turns, which for LGRs = 1, r is radius of the resonator and l is its length. Overall the internal Q factor is given by:

$$Q_{int} = \frac{1}{R}\sqrt{\frac{L}{C}} = \omega_0 \frac{L}{R} \tag{4.3}$$

where R is the resistance and ω_0 is the frequency. This needs to be maximised for best performance. As stated above the capacitance is generally used to select the frequency, this means it can only be reduced so far. The frequency of operation ω_0 is selected, but from equation 4.3 the Q factor reduces for lower frequency resonators. Finally the inductance can be increased. From 4.2 the inductance increases by N^2,

increasing the Q factor, however the resistance is proportional to the length of the circuit, and therefore increases linearly with N. Overall adding turns does increase the Q factor, but this is limited by the length of the solenoid, as increases past a point will result in a reduction in the filling factor, η:

$$\eta = \frac{\int_{sample} |B_1|^2 dV}{\int_{resonator} |B_1|^2 dV} \tag{4.4}$$

where B_1 is the magnetic field produced by the resonator. The filling factor is a measure of the ratio of this magnetic field which is applied to the sample. This can be approximated to be the ratio of the volumes of the resonator and the sample. This must be maximised as a lower filling factor causes an effective reduction in the magnetic field, B_1 experienced by the sample, which results in a smaller signal. This is explained mathematically in equations 5.6 and 5.10. As the sample volume in this case is larger than the volume of the resonator it can be approximated to be 1. But clearly if the volume of the resonator is increased too much then this will no longer be the case.

The Q factor is measured with a NA as per 3.1 and 3.2. This measured Q factor is actually a combination of two different Q factors, internal and external. The internal Q factor represents how long the resonator would oscillate without any loads, with only intrinsic losses. The external Q factor represents the energy lost through the coupling:

$$Q = (\frac{1}{Q_{int}} + \frac{1}{Q_{ext}})^{-1} = \frac{1}{Z + R}\sqrt{\frac{L}{C}} \tag{4.5}$$

Q_{int} and Q_{ext} are the internal and external Q factors, given by:

$$Q_{int} = \frac{1}{R}\sqrt{\frac{L}{C}} \tag{4.6}$$

$$Q_{ext} = \frac{1}{Z_c}\sqrt{\frac{L}{C}} \tag{4.7}$$

The ratio of these two Q factors gives the coupling constant:

$$\beta = \frac{Q_{ext}}{Q_{int}} = \frac{Z_c}{R} \tag{4.8}$$

This constant can be varied by changing the mutual inductance. There are three regions of coupling: undercoupled ($\beta < 1$), overcoupled ($\beta > 1$) and critically coupled ($\beta = 1$). At critical coupling $Q = \frac{Q_{int}}{2}$. This occurs when the impedance of the resonator and coupling loop are matched.

These equations inform us on the properties which can be optimised to try to increase resonator Q factor. Of particular focus is the resistance, from equation 4.6; the resistance should be minimised for the highest possible Q factor, this does not affect the resonant frequency.

4.2 Litz Wire

Litz wire is a multi-stranded wire, in our case made of copper. This wire is of potentially lower resistance than solid copper wire due to a reduction in the skin effect. This is where the current only flows in small area near the outside of the wire. This obviously still occurs in multi-stranded wires however due to larger amount of wires, the overall cross sectional area which current travels through is increased, decreasing the resistance [48]. However these benefits tend to be at lower frequencies, due to the induced currents between strands caused by the proximity effect [49],[48]. It has been shown that adding conductive layers can be beneficial to resonators in the tens of megahertz range [50], although this was not using litz wire specifically and at a slightly lower frequency range. The desired frequency range for our application is high enough that using litz wire may cause greater resistance, but it is also close to ranges where improvements in the resonators have been found. The current flows at a depth known as the skin depth, δ:

$$\delta = \sqrt{\frac{\rho}{\pi \mu_0 f}} \tag{4.9}$$

where ρ is the resistivity, in this case of copper and f is the signal frequency. At the clock transition $f \sim 40$MHz, therefore $\rho \approx 10\mu$m. As this is much smaller than the solid copper wire diameter (0.9mm), multiple strands should decrease the resistance. As such, it was decided to investigate the use of Litz wire for this application. The design was kept as close to the solenoid resonators to allow for easy comparisons, with copper wire simply being substituted for the litz wire.

Two main technical issues were encountered; The first was the removal of the enamel coating. The litz wire is enamelled as otherwise it would not work as separate wires, however, to connect to it, the enamel must be removed from connection points, in our case where the capacitors are added. Various techniques were tried. The most obvious starting point was sanding; this did remove the coating, however, there were several drawbacks. It was time consuming having to sand each strand individually, which was required to ensure good removal; the fine strands were easy to damage; and it was hard to tell whether all coating was actually removed - which also makes it hard to keep track of strands which have been sanded. Acid (etching liquid) was also used. Unfortunately, the acid left a lot of residue and didn't remove all the coating, with a higher than expected resistance meaning sanding was still required to finalise the process, which retained the previous issues albeit to a lesser degree. The final attempted technique was burning the coating off using a small butane torch. This was very effective at removing the coating. A small amount of residue was left however, this was easy to remove with a small amount of gentle sanding, much easier than removing residue left after the acid solution. This was by far the

most effective technique, removing more of the enamel, while also being faster and easier to carry out.

The other technical issue came from the lack of structure of the litz wire. This made making a coil quite difficult. Tape was used to hold it in place during the construction and soldering process. This was quite fiddly and the final result was quite messy. While with more practice it would surely improve, it clearly wasn't the best method. Using a form to wind the wire was a clear way to make the process easier.

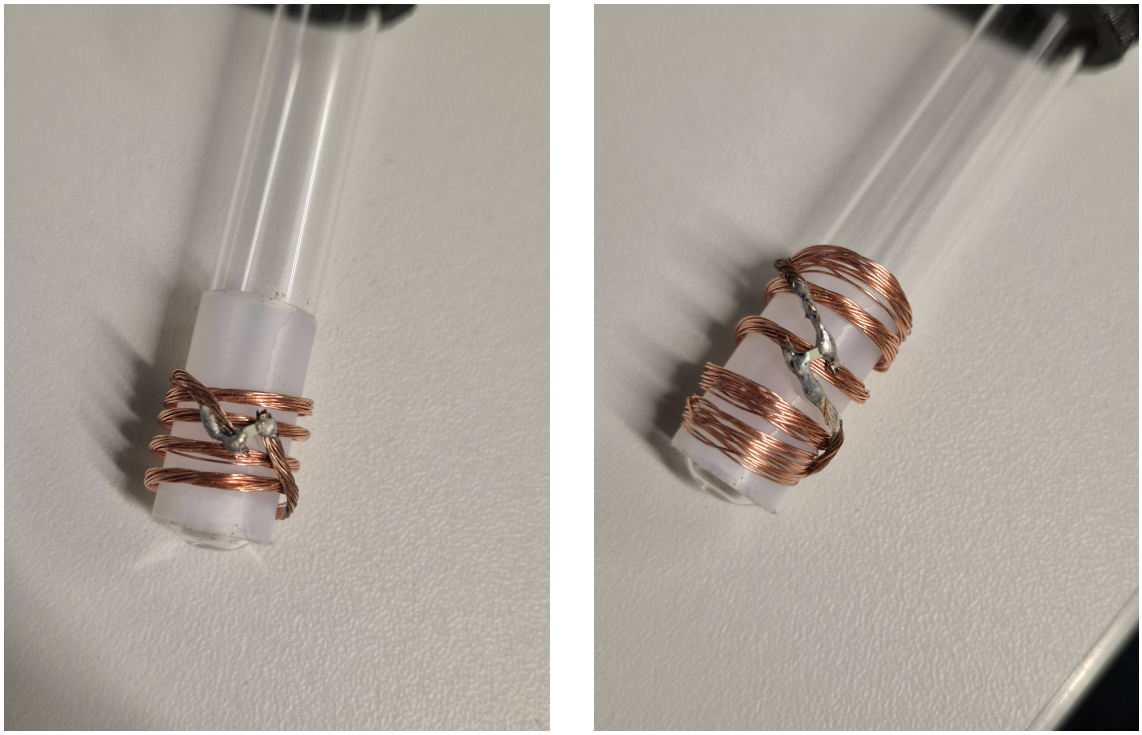

Figure 4.2: Difference between litz wire resonator using form (left) and no form (right)

The form was designed using AutoInventor (more information on this is found in 4.3). The form was extremely helpful in winding the resonators with the grooves holding everything quite securely in place including during soldering. The one caveat is that the form was plastic so care had to be taken while soldering to not burn it. The solder and capacitors add a lot of rigidity to the resonator, with the coil holding its shape much better. This allows them to be removed from the form and be used in the EPR setup.

Measurements of Q factor were taken throughout the design process, and were consistently low, however part of this was due to the suboptimal design. Once an

adequate design and production process was achieved a final Q factor measurement could be carried out. To be able to compare to current solenoid resonators one 82pF capacitor was used, this on a coil resonator usually gives a frequency of around 40MHz, and for the litz wire gave a resonant frequency of 38MHz. Around this frequency coil resonators typically have a Q factor between 100 and 140. Unfortunately, the measured Q factor was much worse than this, with $Q = 44.0$ This is quite disappointing and lower even than loop gap resonators. There are a couple of potential reasons for this. Firstly it is harder to get a good connection to all the strands of the litz wire, and more solder is required to try to achieve this. This increases electrical resistance which decreases Q factor, following equation 4.5. This leads to larger issues is not all the strands are well connected, if some are poorly connected, or not at all, this would result in large differences in electric potential which would cause large amounts of parasitic capacitance between strands further increasing resistance, potentially more than the benefit gained from the theoretical reduction in resistance due to the reduction in skin effect. While these may not be a full explanation for the reduction in Q factor, due to the disappointing results there was no further investigation.

4.3 Form

The form was initially designed to make the construction of the litz wire resonators easier and was very effective for this, making the process reasonable. Shown in figure 4.3 is the first prototype, however, this ended up being almost exactly what was required so no further iteration was made. The form has spiral grooves on each end for the wire to be wrapped around and then easily removed by simply rotating them off the end. The ends have different shapes: one has deeper grooves and a larger groove spacing than the other. This allowed for easy construction and investigation of two differently shaped coils.

The form was not just useful for the litz wire though, having a structure to work the copper wire into made making conventional solenoid resonators much easier. It also lead to greater consistency between resonators and more reliably produced an evenly spaced coil than hand winding. The obvious downside to this is you have less control over the final shape. Overall this is a price worth paying particularly for the easier making process. Unfortunately the more consistent coils do not lead to a significant change in Q factor, with measured Q factors ranging between 100-140. This is consistent with the hand wound resonators at similar frequencies (around 40MHz). Overall the forms are definitely worth using due to the increased ease in making the solenoids.

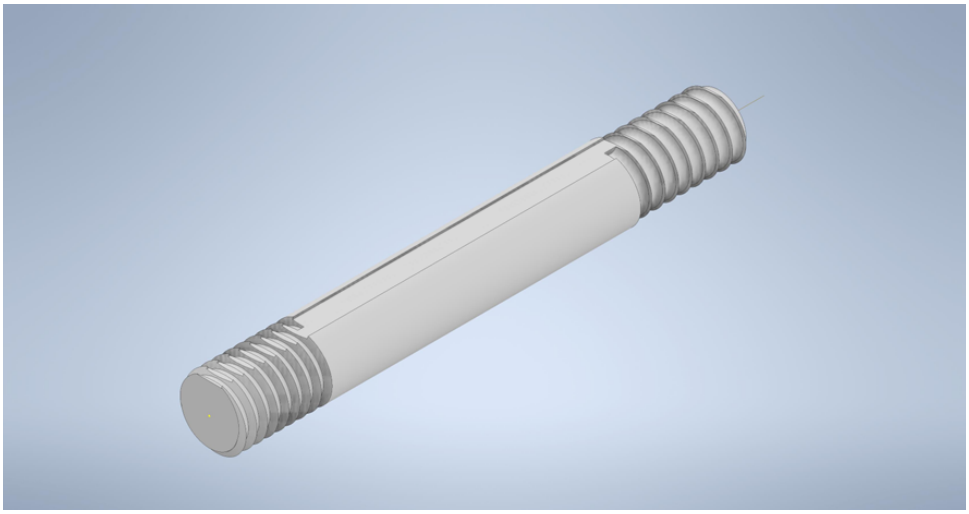

Figure 4.3: Resonator form modelled in AutoInventor 3D

4.4 3D Printed Resonators

Finally an investigation into using 3D printed resonators was carried out. While these don't offer an intrinsic improvement they offer a far greater range of possible designs than can be produced by hand winding or winding using a form. 3D printing opens the door to all sorts of potential designs: different wire cross sections as seen in figure 4.4, toroidal resonators, double resonators and more. These resonators are 3D printed in plastic then painted with graphite paint to allow a conducting copper layer to be electroplated on. The coils were designed by Prof. Edward Laird and then made by Marthur Kartikey and Andrew Kennedy from the engineering department at Lancaster University. These were received as coils so still required capacitors. As with the litz wire resonators a 82pF capacitor was chosen as it should give a frequency within the range of our current resonators making the Q factor easier to compare between them. Unfortunately soldering the capacitors was not an option as the coating likely could not handle the heat; this gave us several options.

The first of these was silver paint. Initially there were issues with adhesion as the physical connection was very weak, however later it was realised that this was due to user error; the paint was not shaken thoroughly enough before application, resulting in a more watery and weaker application. With proper application the connection was secure enough, although still delicate. Next silver epoxy was also used, this is a two-part epoxy which has to be mixed up in even quantities and then applied. Due to the small amount required this process is quite wasteful as getting small and even amounts out of the tube is difficult and inevitably ends up with wasted epoxy. The epoxy did work well, giving a strong and conductive bond. Finally solder paste was

tried as this should melt at a lower temperature than solder. The exact temperature that the coating can handle is unknown so care was taken throughout this process. Rather than using a soldering iron a heat gun was used to hopefully be gentler on the coil, however this may have not been the case. A successful connection was made on one arm but on the other the solder was still a paste, heating was continued but the resonator violently split into a few pieces. The resonator could not withstand the stresses caused by the heat gun. The best of these options is silver paint; it is the easiest to use and apply as well as being less wasteful than the epoxy.

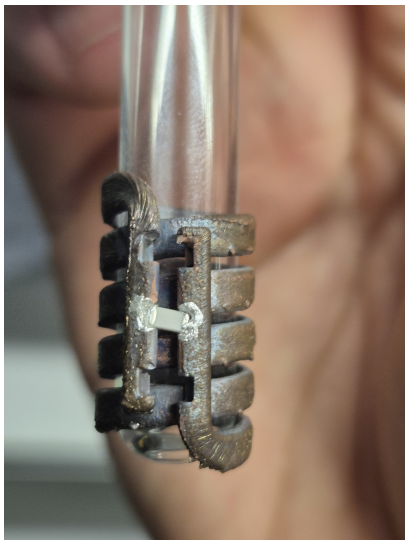

Figure 4.4: 3D printed resonator with capacitor attached with silver paint

Once capacitors had been attached to the remaining coils, measurements of their Q factors were attempted using the NA. Unfortunately only one could be measured. Two were too large to fit into the spectrometer fully. To attempt to take a reading the top of the spectrometer box was removed and the coupling loop was raised as much as possible, allowing for a measurement to be made by resting the resonator on the upper lip. Unfortunately no resonance was able to be seen on either resonator; one had a clearly damaged connection, the other visibly looked fine however the connection may have been damaged or there may have been an issue with the continuity of the coating. The final resonator did fit into the spectrometer and the Q factor was successfully measured, Q = 40 at 45MHz. This is much lower than the standard solenoid resonators, and a bit lower than LGRs for this frequency. However this was only the first prototype.

A second set was provided with a slightly altered design, shown in 4.4. These had thicker and taller walls, providing more stiffness and a thicker conducting layer, which should improve the Q factor due to lower resistance. Small notches were

also added to make attaching capacitors easier and also increase surface area of the connection, hopefully gaining better conductive contact, leading to an increased Q factor. These notches should also give more structural strength to the connection due to the larger surface area. These still were slightly too wide to fit into the coupling loop. To counteract this a small separate set up was made to measure their Q factors. This was made of a coupling loop which was removed from an old set up and held in place by a component holder. To make sure the setup was stable enough for an accurate reading, a resonator with known Q factor was tested. The original Q factor was 104, and the measured was 101, a negligible difference, especially considering that it is difficult to achieve identical coupling between different tests. We had two resonators with this new design and again attached 82pF capacitors.

Q factors were again measured with the VNA; coil 1, (C1) achieved very strong coupling (-70dB) however had a low Q factor of 32. Coil 2 (C2) had very weak coupling, with a maximum achieved of -5dB and a very low Q factor of 20. This is clearly not an improvement and just generally a very poor result. The silver paint does recommend annealing in an oven after leaving it to air dry for the best electrical and mechanical results. This was carried out after the initial measuring in case this damaged them. The recommended temperature for the paint is 120°C for 10 minutes, however we were recommended to not go above 60°C due to the possibility of delamination between the layers of the coil. Given this both resonators were put in the oven for 30 minutes at 60°C to hopefully achieve a similar result to what would be seen from the recommended temperature. Unfortunately C2 did not survive the oven; the capacitor lost connection on both sides. Due to its poor original Q factor no attempt was made to repair this. C1 did survive and did actually see an increase in Q factor to 36. While some of this may be variation between tests it is possible that the oven may have helped. However this Q factor is still below LGRs and far below the hand wound solenoids.

The final thing to try with 3D printed resonators is solder. This was initially avoided due to the high temperatures required, likely causing damage to the coils. However a final set of coils were made with heat resistant resin, able to tolerate up to 200°C, making it much more likely to survive the soldering. Two coils were provided, one was able to be soldered completely fine, unfortunately the other had a large flake of the conductive coating come off, ruining the resonator. Unfortunately the resonator which had been successfully soldered had no measurable resonance. This wasn't completely surprising as with previous methods some resonators had also not been measurable for no visible reason. It is suspected that inconsistencies in the coating lead to high resistance in certain zones ruining the Q factor and potentially causing breaks in continuity. At this stage the work on 3D printed resonators was halted. The consistently low Q factors, inconsistency and difficulty in manufacturing made

any further work at this time not seem worth it, especially as these issues would make producing more consistently good coils a challenge.

While litz wire and 3D printed resonators offered potential benefits, the very poor Q factors which both demonstrated mean that neither are suitable alternatives to the already developed LGRs and solenoid resonators. In the process of developing the litz wire resonators a form was designed; this ended up being very useful for conventional solenoid resonators, one of which was used to produce the CW EPR results shown in 5.1.

Chapter 5

Results

5.1 CW EPR

Before beginning on pulsed EPR some time was spent on CW EPR to gain experience with similar and simpler equipment and code. It is also useful to understand CW EPR for two reasons, firstly it makes it easier to understand pulsed EPR, secondly the group's clock is currently envisioned to use CW. Initial measurements were run using DPPH (2,2-diphenyl-1-picrylhydrazyl). This one of the most widely used EPR standards [51] and importantly has a much stronger EPR signal than $^{15}N@C_{60}$, making measurements easier to acquire. Once this was successfully carried out the sample was switched to $^{15}N@C_{60}$. While having a weaker EPR signal this was also measured. This was done in parallel mode at 52.8MHz.

While not novel the results shown in figure 5.1 demonstrate a successful EPR measurement. This was done in parallel as parallel mode is of more interest due to the presence of a clock transition explained in section 2.0.1. The frequency was used as the resonator had worked well for the DPPH measurement so was carried over. The signal here is the DC voltage recorded at the lock-in amplifier, the magnitude of which depends on the amount of signal reflected from the resonator. The X-Phase and Y-Phase are the signals at the two phase sensitive detectors of the lock-in amplifier. The reason for the small spike in the Y-Phase graph is due to imperfect phase, resulting in a small amount remain in the X-Phase. While this could have been corrected for, given that this still shows a successful EPR measurement of $N@C_{60}$ this was not a priority. Similarly a measurement at the clock transition could have also been taken this was also not deemed important as it has been done before; time was better spent working towards pulsed EPR.

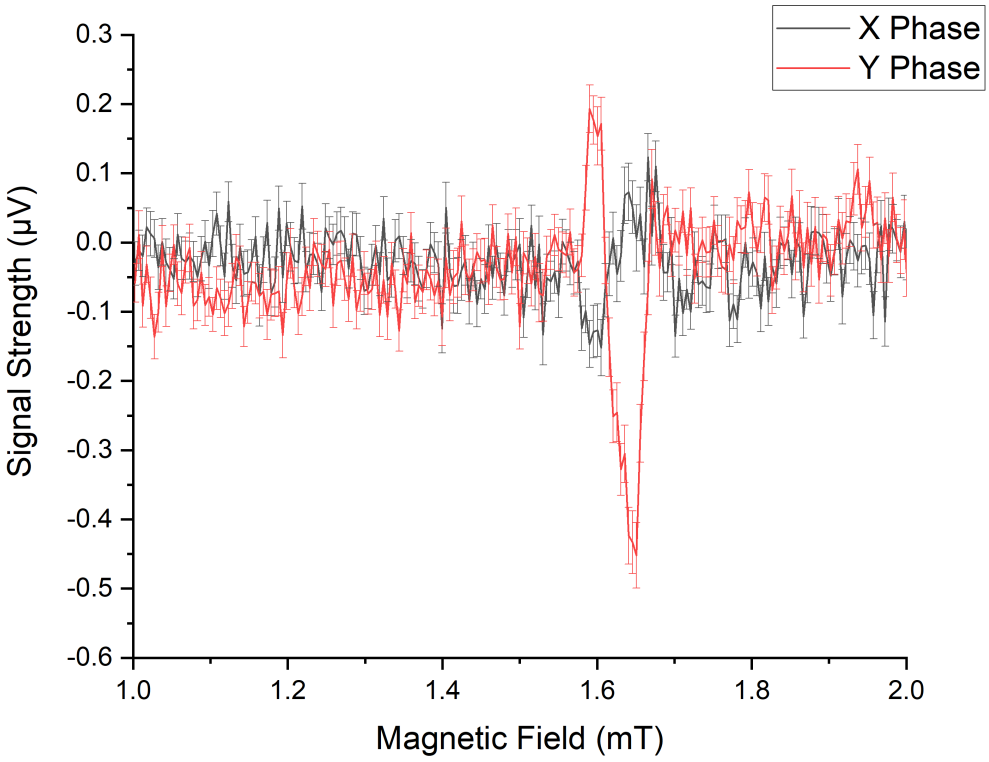

Figure 5.1: CW EPR measurement of $^{15}N@C_{60}$ at 52.8MHz

5.2 Pulsed EPR

5.2.1 Perpendicular Mode Operation

Similarly to what was done in CW a material with higher EPR response was used to begin with rather than $^{15}N@C_{60}$. This was LiPc (Lithium Pthalocyanine). Measurements were started in perpendicular for two reasons. Firstly LiPc has no EPR response in parallel mode, secondly for $^{15}N@C_{60}$ only perpendicular mode has been able to be measured in this frequency range. It was very useful to start with LiPc as initially difficulties were encountered. The much stronger signal made it easier to see a small result from which the signal could then be optimised. Once this was done the sample was switched to $^{15}N@C_{60}$ for this to be investigated.

$^{15}N@C_{60}$ transitions were eventually found. The considerably reduced signal strength required a lot of optimisation to be visible, particularly the timings for the switches and duration of the pulses. This eventually lead to data shown in figure 5.2.

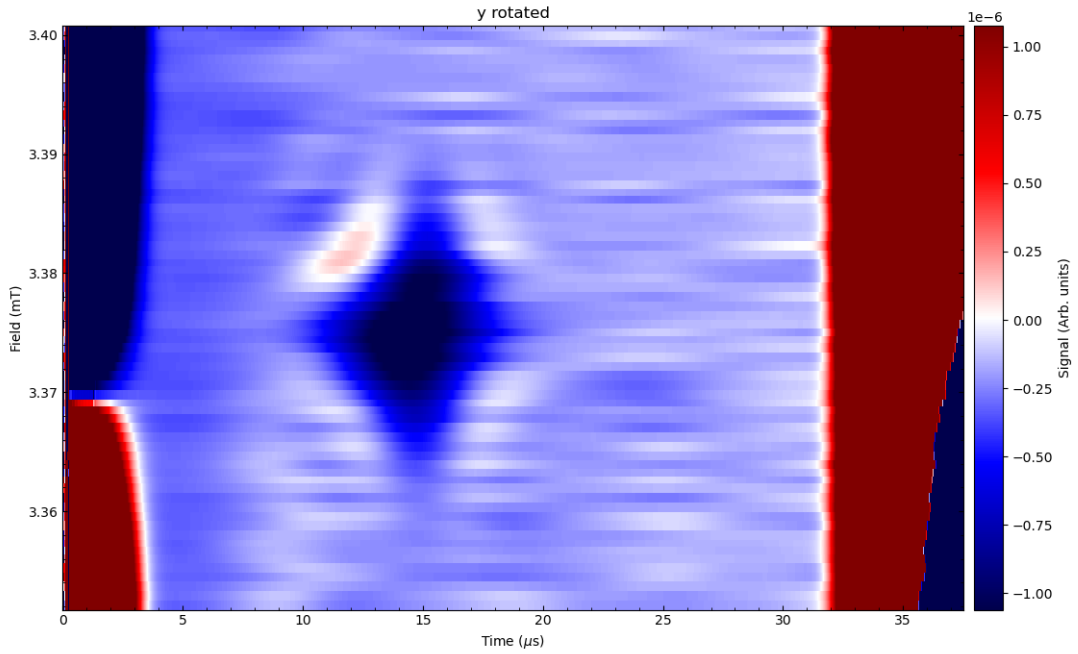

Figure 5.2: Example of successful echo measurement at 3.375mT with 7μs separation time

This shows a very strong echo at the field strength expected for the frequency. This was measured at 120MHz. The increased frequency was helpful when optimising due to the increased signal strength at higher frequencies. While this data shows a strong response the aim of this project was to measure at lower frequencies, as well as in parallel mode. Next measurements were taken at 60MHz and used to create an estimate for T_2 time. 60MHz was chosen as there are two transitions present near 2mT. This is useful as within one scan it allows for two different T_2 times to be found. To find the T_2 time multiple pulse separations are required, these can be seen on figure 5.3. Before 10μs any potential echo is obscured by the noise from the ring-down and the video noise from the switching. The echo appears at double the separation plus a small amount of time at the beginning of the sequence, giving 5μs as the lower limit. The upper limit of separation time is from the echo signal reducing in strength as explained in section 2.0.3. Finally the π duration was optimised to be 40ns for this transition.

To find T_2 from this plot the following equation is used:

$$V = V_0 e^{-2\tau/T_2} \tag{5.1}$$

where V is signal intensity at time τ. This is the Hahn separation and is the time between the pulses, V_0 is the signal intensity at zero seconds so no spin-lattice

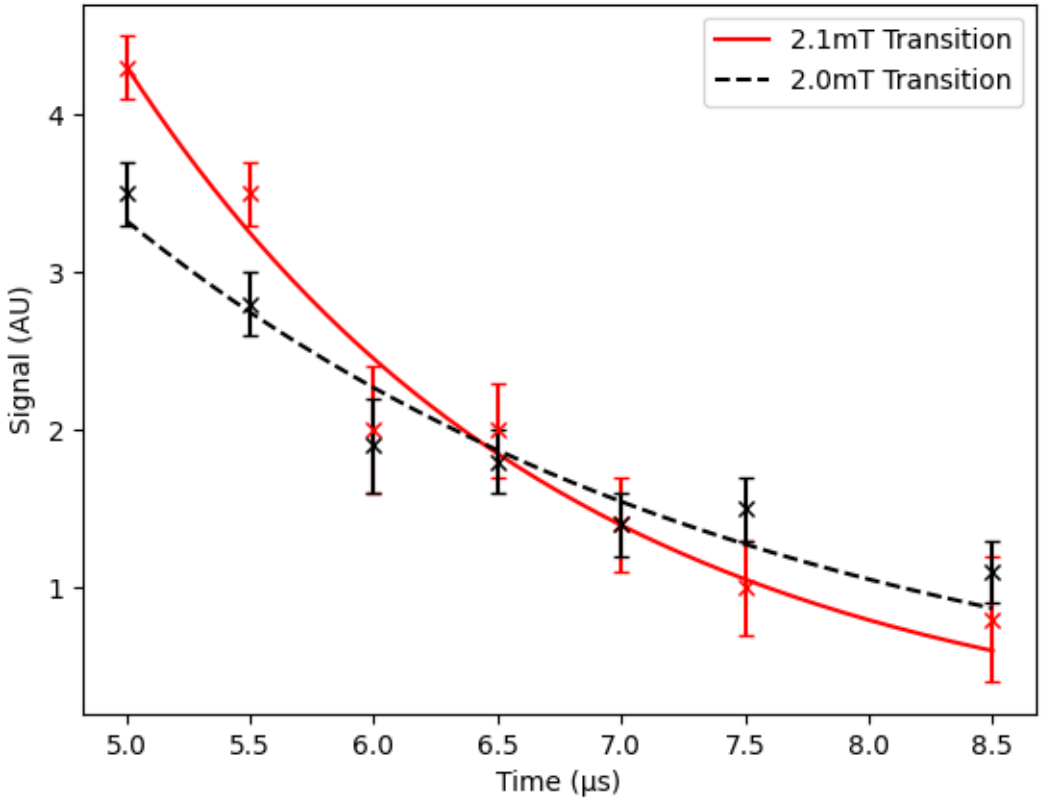

Figure 5.3: T_2 measurement at 60MHz for 2.1mT and 2.025mT Transitions

relaxation occurs. The lines are fitted according to this equation and we obtain two values for T_2 corresponding to each transition. These are $3.9 \pm 0.5\mu$s and $5 \pm 1\mu$s, for 2.1mT and 2.0mT respectively. These values can then be used to estimate an Allan deviation using equation 2.16. First the frequency linewidth, $\delta\omega$ must be found using 2.17. For 2.1mT $\delta\omega = 80 \pm 10$kHz, for 2.0mT $\delta\omega = 60 \pm 10$kHz. We can compare these values to those found by Harding et al. [29] who used a fit to estimate the linewidth at the clock transition (38.6MHz) and found $\delta\omega \approx$100kHz. It is expected that the linewidth narrows towards clock transition although no measurements at the transition have been made. The lowest measurement before this was carried out by M. Green [30] at 102 MHz and found a linewidth of $\delta\omega = 37 \pm 3$kHz. The measurements gathered in this study align more with the values gathered from the clock transition map from Harding et al. however as there was no measurement made at the clock transition whether the data fully agrees is not yet known.

From 2.18 a value for Q can be found using $\delta\omega$, which can then substituted into 2.16

to find the Allan deviation. As an estimation for the Allan deviation is desired at the clock transition the frequency ω used to calculate Q is 38.6kHz. To complete the Allan deviation estimate a S/N ratio is required; unfortunately there was not enough time for this to be measured in this configuration therefore a value has to be chosen. There are two potential values for this, from Harding et al, or Green. The equipment used was very similar to that used by Green, and the biggest improvements in S/N by Green compared to Harding et al. apply in this set up. These were an increase in filling factor from 0.6875 to 1 due to increased sample volume, and an increase in spin concentration from 6000ppm to 22000ppm. Therefore Green's S/N ratio of 9.16 $\text{Hz}^{\frac{1}{2}}$ was used.

Using these values gives $\sigma_y(\tau) = 2.2 \pm 0.3 \times 10^{-4}\tau^{-1/2}$ for 2.1mT and $\sigma_y(\tau) = 1.6 \pm 0.3 \times 10^{-4}\tau^{-1/2}$ for 2.0mT. This is an improvement in Allan deviation estimate compared to Harding's of $1.3 \times 10^{-3}\tau^{-\frac{1}{2}}$ but worse compared to Green's estimate of $9.5 \times 10^{-5}\tau^{-\frac{1}{2}}$. This increase stems from the increase in $\delta\omega$ - in theory this should be lower providing an improved Allan deviation estimate however this is not what was found. The estimate made in this project is still much worse than current CSACs, these are on the order of $\times 10^{-10}$ as per 1.3. At the time of writing this is the lowest frequency measurement of T_2 time in $^{15}N@C_{60}$. Ideally it would have been useful to measure closer to the clock transition, however especially for longer Hahn separation times the S/N ratio was quite poor, and was approaching the limit of what was useable, and this would only get worse at lower frequencies. To do this improvements to the S/N ratio must be made, and an investigation into the potential problems was carried out.

It should be pointed out that the S/N ratio was assumed to have remained constant between the two measurements and set ups. While these were not dramatically different there were changes. Furthermore an investigation was carried out into the noise of the system and this was found to be worse than expected; further details in section 5.2.3.

5.2.2 Parallel Mode Operation

While various improvements were made to the set up as per 3.2.1 a good enough signal to be used to estimate T_2 was not able to be measured. This was expected to be harder to measure due to weaker expected signal, requiring a better S/N ratio. The signal has to be clearly above the noise for an accurate value of signal intensity to be measured. This was not able to be achieved for short Hahn separations and would be more of an issue at longer Hahn separations. To understand the issue an investigation into both the noise and theoretical signal was carried out.

5.2.3 Noise investigation

The S/N ratio was not good enough in parallel mode and as stated previously approaching the limit of usability in perpendicular mode. This provides two areas for investigation, the theoretical signal and noise. If the expected noise is different to the measured noise then it might inform where any potential issue may lie, while the theoretical signal and its value compared to both the expected and measured noise could inform whether the setup as a whole is likely to work or whether larger changes are required.

Firstly the theoretical noise was calculated and compared to the noise measured using a spectrum analyser. To find the noise the Friis equation [52] is used:

$$T_{N,A} = T_{N,A_x} + \frac{T_{N,A_{x+1}}}{G_x^2} + \frac{T_{N,A_{x+2}}}{(G_x G_{x+1})^2} + ... \tag{5.2}$$

where $T_{N,A}$ is the noise temperature of the system, and T_{N,A_x} and G_x are the noise temperature and gain for each respective component. These values are taken from the data sheet but require a conversion using $G = 10^{G_{dB}/20}$ and $T_N = T_0(10^{F_{dB}/10} - 1)$ respectively. For the shielding switch these values are $G = 0.9$ and $T_N = 69$K. For the two switches $G = 17.8$ and $T_N = 44$K. These values are both at 100MHz as this was the frequency at which measurements were attempted. While there are more than three components in the circuit only these three are required for the Friis equation. Anything following these adds a negligible amount due to the increasing denominator for increasing terms. The measurement using the spectrum analyser was taken at the output of the amplifiers. Furthermore the only component present before the shielding switch was the directing switch whose noise is shielded by the shielding switch.

Substituting these values into the Friis equation $T_{N,A} = 124$K. This is the noise added by the components, therefore the noise floor is this plus room temperature, $T_{N,system} = 424$K, for a room temperature of 300K. Finally to be compared to the spectrum analyser result this must be converted into spectrum density using:

$$S_{VV}^N = kZ_0 T_{N,system} \tag{5.3}$$

This gives us the input referred noise, $S_{VV}^N = 2.93 \times 10^{-19}$V/Hz. This must be multiplied by the gain of the chain up to the output of the last amplifier, $G = 285$, and converting to noise power density $P_N = 1.67 \times 10^{-18}$W/Hz. This can be compared with the measured value found with a spectrum analyser also at the input to the mixer. Using the analyser the noise was measured to be -81dBm in a bandwidth of 100kHz, which converts to $P_N = 7.94 \times 10^{-17}$W/Hz. The measured value is clearly much higher than the theoretical noise floor of the system so should

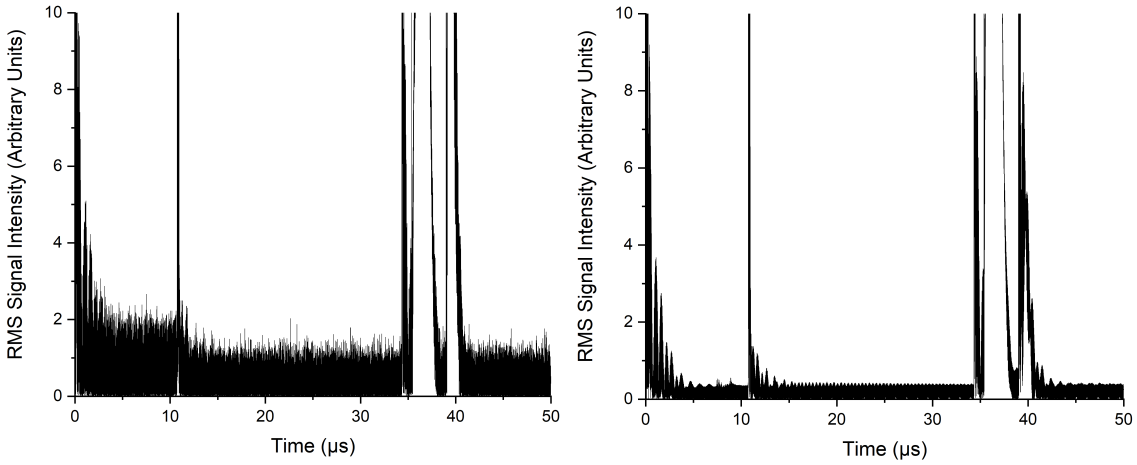

Figure 5.4: RMS noise against time for 1 measurement (left), 10000 measurements (right)

be able to be improved considerably. Unfortunately there was not enough time to identify why this was the case; the individual components were behaving as expected when tested in isolation.

5.2.4 Averaging Investigation

The effect of noise can be reduced by averaging over many measurements, with an expected reduction by a factor of $\frac{1}{\sqrt{N}}$ for N measurements. However the observed noise reduction factor was smaller than was expected therefore an investigation into this was also carried out. This was done by measuring the signal at a single magnetic field strength and comparing the results for one measurement against an average of 10000 measurements. Graphs of the RMS signal intensity against time were used to compare the two cases, shown in figure 5.4.

It is important to not simply take the average of the full graph as this would include spikes in signal due to the video noise from the switches. This noise is not present in the measurement zone so needs to be ignored. The zone chosen was from 13-34μs. Other regions later in the measurement could also be used, however this is the region in which an echo would be present, so is of most interest. Before finding the RMS the mean of the values in the range must first be subtracted to remove any potential offset. The RMS is then calculated as after subtracting the mean the remaining values are distributed above and below 0.

The average RMS from 13-34μs is RMS = 0.412$\pm$0.002 AU, and for 10000, 0.201 $\pm$ 0.001 AU. These errors were calculated using $\frac{\sigma}{\sqrt{n}}$, where σ is the standard deviation

in the mean and n is the number of points used (29400). From these numbers we can see a clear reduction in noise with an increasing number of measurements, however this decrease is much smaller than expected. The noise is expected to be white noise, and therefore decrease by a factor of $\sqrt{N}$ with N being number of measurements. Going from 1 to 10000 measurements this should reduce noise by a factor of 100; instead a factor of roughly 2 is seen. Clearly this is not what was expected, the noise is not being averaged down as it should be. The exact cause for this is not known and due to time constraints was unfortunately not able to be investigated.

5.2.5 Theoretical Echo Signal

Along side both the measured and expected noise it would be very useful to calculate the expected signal. This can tell us whether the signal produced is as expected and if it is then whether the experiment is feasible in its current state or whether larger changes are required. If the theoretical signal is below the theoretical sensitivity of the system then larger changes are definitely required. To do this a method from Rinard et al. [53] was followed:

The voltage induced in resonator is:

$$V_s = n\frac{d\phi_0}{dt} \tag{5.4}$$

where n is the number of resonator turns (for a LGR $n = 1$), and ϕ_0 is the magnetic flux produced by the magnetisation of the sample and is given by:

$$\phi_0 = \mu_0 \eta \mathbf{A} \cdot \mathbf{M_0} \tag{5.5}$$

where $\mu_0 = 4\pi \times 10^{-7} Hm^{-1}$, the vacuum magnetic permeability constant, η is the filling factor (4.4) and ≈ 1 in this case as the volume of the solution is always larger than the volume of the resonator, $\mathbf{A}$ is the cross sectional area of the resonator, and $\mathbf{M_0}$ is the magnetisation of the sample and varies sinusoidally with frequency, ω_0. The magnetisation is assumed to be fully on the xy plane, as the pulse duration used is less than $\frac{1}{T_2^*}$. Therefore the peak voltage is given by:

$$V_s = \mu_0 \eta A M_0 \omega_0 \tag{5.6}$$

where ω_0 is the frequency; for this calculation it is 100MHz. As with the noise calculation this value was chosen as it was where the parallel measurements took place. The magnetisation of the sample is given by:

$$M_0 = N\frac{\gamma^2 \hbar^2 B_0}{4k_B T} \tag{5.7}$$

where N is the spin concentration, γ is the gyromagnetic ratio, $\hbar$ is the reduced Planck constant, B_0 is the magnetic field, k_B is the Boltzmann constant and T is the temperature, 300K.

Assuming all spins are magnetised the peak voltage in Pulsed EPR is given by:

$$V_0 = \frac{\sqrt{\beta}}{\beta + 1}\sqrt{\frac{Z_0}{R}}V_s \tag{5.8}$$

where Z_0 is the impedance of the line, 50Ω, R is the resistance of the resonator and β is a measure of the coupling and equal to:

$$\beta = \frac{2Q_C}{Q_O} - 1 \tag{5.9}$$

where Q_C is the Q value at critical coupling and Q_O is the overcoupled Q value used in the experiment. Substituting in equations 5.6 and 5.7 gives an expected voltage:

$$V_0 = \frac{\beta}{1 + \beta}\sqrt{\frac{Z_0}{R}}N\frac{\mu_0\eta A\omega_0\gamma^2\hbar^2 B_0}{4k_B T} \tag{5.10}$$

There are several values within this which need calculating or measuring. The cross sectional area requires the radius which was found by measuring the diamter with calipers giving $A = 1.21 \times 10^{-4}\text{m}^3$. To calculate β two Q factors are needed and were measured in the same way as explained in section 3.1. These were found to be $Q_C = 103$ and $Q_O = 58$, giving $\beta = 2.55$. R needs to be calculated using $R = \frac{\omega_0 L}{Q_{int}}$ where Q_{int} is the internal Q factor and is found using $Q_{int} = 2Q_c$. The inductance, L follows equation 4.2 and is then substituted in giving $R = 5.53 \times 10^{-4}\Omega$. η as stated earlier is simply 1 in an LGR. The frequency, ω_0 specifies the field according to the transition map, in this case $B_0 = 2.5\text{mT}$. N must be calculated. The sample in use has 22000ppm of $N@C_{60}$ in C_{60}. The sample was made with approximately 1.5mg of solid, giving 2.76×10^{16} spins. This was dissolved in CS_2 which was then allowed to evaporate to reach the solubility limit. This is 7.9mg/ml at room temperature [54]. Combining these gives a spin concentration, $N = 1.46 \times 10^{17}\text{cm}^{-3}$. Finally γ is the gyromagnetic ratio and can be substituted using $\gamma = \frac{\omega}{B_0}$. Combining all of these gives a theoretical signal, $V_0 = 1.52 \times 10^{-17}\text{V}$ in the resonator. This is an extremely small voltage and would not be measurable in the current set up. While this could be correct it is more likely that the model used is not applicable here. We can check this by repeating the calculation using the frequency and resonator of a successful measurement. For example using those of the data to produce 5.3. Using these gives $V_0 = 1.45 \times 10^{-18}$. It is expected that the signal decreases with frequency, so it makes sense that this second result is lower as it is at 65MHz rather than 100MHz, however this would also not be measurable but in practice it was. Therefore we

can conclude that in this case this method is not suitable to calculate the expected signal. A very useful next step would be to find or develop an applicable way to calculate as it would allow for a prediction of S/N ratio to be made which would increase understanding of the feasibility of project.

Chapter 6

Conclusions

The main goal for this project was a measurement of the T_2 relaxation value at lower frequencies than had been done before. Along side this an investigation into potential new techniques in resonator design was carried out with the hopes of increasing resonator performance, particularly increasing Q factors.

Both 3D printed and litz wire resonators had much lower measured Q factors than LGR and solenoid resonators. litz wires suffer from increased electrical resistance either due to poor electrical connection or parasitic capacitance effects. While 3D printed resonators offer potential benefits in design, the increased resistance compared to copper wire prevents these from being useful at this point. The form design for use with litz wires turned out to be extremely useful, making the construction of solenoid resonators a much easier process and producing more consistent coils. This is a partial success in improving resonator design, while better Q factors were not achieved, the manufacturing process has been improved.

Successful pulsed EPR measurements were taken. These were used to find the T_2 relaxation time of $^{15}N@C_{60}$ at the lowest currently measured frequency (60MHz). These were found to be $3.9 \pm 0.5\mu$s and $5 \pm 1\mu$s for 2.1mT and 2.0mT transitions respectively. These were converted to linewidth values, $\delta\omega = 80 \pm 10$kHz (2.1mT) and $\delta\omega = 60 \pm 10$kHz (2.0mT). The linewidth at the clock transition is expected to narrow, so assuming that the linewidth is at least this narrow an estimation can be made of the Allan deviation. These were found to be $\sigma_y(\tau) = 2.2 \pm 0.3 \times 10^{-4}\tau^{1/2}$ for 2.1mT and $\sigma_y(\tau) = 1.6 \pm 0.3 \times 10^{-4}\tau^{1/2}$ for 2.0mT. While an improvement in comparison to Harding's estimation [29], this was mainly due to an improvement in the S/N ratio used, rather than a lower intrinsic linewidth measurement. Currently this estimation is much worse than other CSACs or quartz oscillators. However clearly there is uncertainty on the linewidth at the clock transition. This has not

yet been successfully measured and for a more accurate estimation to be made this is required and should be a clear focus for future work.

While carrying out the pulsed EPR measurements issues with the signal-to-noise (S/N) ratio were encountered. This lead to a noise investigation where the noise was measured to be higher than predicted, as well as not reducing as much as expected with averaging. The theoretical noise was calculated to be, $P_N = 1.67 \times 10^{-18}$W/Hz, approximately 50 times lower than the measured noise. The averaging also produced unexpected results, with 10000 averages only reducing noise by a factor of 2 rather than the expected 100. Time constraints meant that the causes of these could not be properly investigated, however if these could be fixed they would offer very large improvements in the S/N ratio of the setup. This would offer a better value for Allan deviation and allow for measurements to be made at lower frequencies and potentially at the clock transition in parallel.

The theoretical signal was also calculated, however the method used was clearly not applicable due to the very low voltage found, on the order $\times 10^{-17} - \times 10^{-18}$. This would result in a voltage too low to be measurable but in practice it was, so this method was not suitable. A working model would be useful in determining the feasibility of the set up, or whether larger changes are required. However the first priority should be understanding why the measured noise is higher than suggested by theory and why averaging is not reducing noise by as much as expected.

Future work should be focussed on investigating the S/N ratio so that measurements can be made at lower frequencies and in parallel mode so that the 'clock transition' can be studied. An improvement in signal strength could be obtained from a better sample, with higher purity. This however would be more expensive. A solvent with higher solubility would also offer an increased signal strength, and should be investigated. Finally at the current moment solenoid and LGRs appear to be the best types of resonators for the frequencies under investigation. The form made here was a prototype and worked very effectively in making consistent solenoids; this should be optimised, maximising the Q factor of the produced resonators by controlling their physical properties.

Appendix A

Full equipment list used in pulsed EPR:

Signal generator providing reference frequency for mixing: Rigol DSG815

Splitter: Mini-Circuits ZMSCQ-2-120+

Mixers: Mini-Circuits ZP-5MH-S+

Low Pass filters: Mini-Circuits SBLP39+ DC-23MHz

Splitter: Mini-Circuits ZECS-2-11+

Amplifiers: Mini-Circuits ZX60-P103LN+

Amplifier DC power supply: TENMA T2-10505

Network Analyser: Copper Mountain S5048

Pre-spectrometer Amplifier: EIN 510L RF power amplifer – 9.5W (45dB)

Helmholtz DC power supply: Keithley 2280S-32-6

Signal generator: Rigol DSG836A

Arbitrary waveform generator: Zurich instruments HDAWG 2.4GSa/S, 16bit

Limiters: Mini-Circuits VLM-33-S+

Shielding switch: Mini-Circuits ZSWA4-63DR+

Directing switch: RF-Lambda – RFSP2TRDC06G

Digitiser card: AlazarTech ATS9440

Bibliography

1. Lombardi MA, Novick AN, Neville-Neil G, and Cooke B. Accurate, Traceable, and Verifiable Time Synchronization for World Financial Markets. eng. Journal of research of the National Institute of Standards and Technology 2016; 121:436–63
2. Vodolazhskaya L, Larenok P, and Nevskiy M. Ancient astronomical instrument from Srubna burial of kurgan field Tavriya-1 (Northern Black Sea Coast). eng. 2014
3. Balmer RT. The operation of sand clocks and their medieval development. Technology and Culture 1978; 19:615–32
4. Lepschy A, Mian G, and Viaro U. Feedback control in ancient water and mechanical clocks. IEEE Transactions on Education 1992; 35:3–10. DOI: 10.1109/13.123411
5. Brearley HC. Time telling through the ages. Doubleday, Page & Company, 1919
6. Blumenthal AS and Nosonovsky M. Friction and Dynamics of Verge and Foliot: How the Invention of the Pendulum Made Clocks Much More Accurate. Applied Mechanics 2020; 1:111–22. DOI: 10.3390/applmech1020008. Available from: https://www.mdpi.com/2673-3161/1/2/8
7. Glennie P and Thrift N. Shaping the Day: A History of Timekeeping in England and Wales 1300-1800. eng. 1st ed. United Kingdom: Oxford University Press, 2009 :40–2
8. Bennett M, Schatz MF, Rockwood H, and Wiesenfeld K. Huygens's clocks. eng. Proceedings of the Royal Society. A, Mathematical, physical, and engineering sciences 2002; 458:563–79
9. Cipolla CM. Clocks and culture, 1300-1700. WW Norton & Company, 2003
10. Yoder JG. Chapter 3 - Christiaan Huygens, book on the pendulum clock (1673). *Landmark Writings in Western Mathematics 1640-1940*. Ed. by Grattan-Guinness I, Cooke R, Corry L, Crépel P, and Guicciardini N. Amsterdam: Elsevier Science, 2005 :33–45. DOI: https://doi.org/10.1016/B978-

044450871-3/50084-X. Available from: https://www.sciencedirect.com/science/article/pii/B978044450871350084X

11. Forbes EG. The origin and development of the marine chronometer. Annals of Science 1966; 22:1–25. DOI: 10.1080/00033796600203005. eprint: https://doi.org/10.1080/00033796600203005. Available from: https://doi.org/10.1080/00033796600203005
12. De Grijs R and Institute of Physics (Great Britain) p. Time and time again : determination of longitude at sea in the 17th century. eng. Bristol [England] (Temple Circus, Temple Way, Bristol BS1 6HG, UK), 2017
13. Howe H. The story of Greenwich time. Journal of the British Astronomical Association, Vol. 80, pp. 208-211 1970; 80:208–11
14. Margolis H. A brief history of timekeeping. Physics World 2018 Nov; 31:27. DOI: 10.1088/2058-7058/31/11/36. Available from: https://dx.doi.org/10.1088/2058-7058/31/11/36
15. Lombardi MA. The evolution of time measurement, Part 2: quartz clocks [Recalibration]. IEEE Instrumentation Measurement Magazine 2011 Oct; 14:41–8. DOI: 10.1109/MIM.2011.6041381
16. Katzir S. Pursuing frequency standards and control: the invention of quartz clock technologies. eng. Annals of science 2016; 73:1–39
17. Lombardi M. The evolution of time measurement, Part 2: quartz clocks [Recalibration]. IEEE Instrumentation Measurement Magazine - IEEE INSTRUM MEAS MAG 2011 Oct; 14:41–8. DOI: 10.1109/MIM.2011.6041381
18. Vig JR. Tutorial Session 1B - Introduction to Quartz Frequency Standards. eng. *2006 IEEE International Frequency Control Symposium and Exposition*. IEEE, 2006 :nil18–nil18
19. Lyons H. The Atomic Clock: A Universal Standard of Frequency and Time. The American Scholar 1950; 19:159–68. Available from: http://www.jstor.org/stable/41205288 [Accessed on: 2025 Sep 27]
20. Lyons H and Husten BF. The atomic clock. United States Patent Office, 1955
21. Beloy K, Bodine MI, Bothwell T, Brewer SM, Bromley SL, Chen JS, Deschênes JD, Diddams SA, Fasano RJ, Fortier TM, Hassan YS, Hume DB, Kedar D, Kennedy CJ, Khader I, Koepke A, Leibrandt DR, Leopardi H, Ludlow AD, McGrew WF, Milner WR, Newbury NR, Nicolodi D, Oelker E, Parker TE, Robinson JM, Romisch S, Schäffer SA, Sherman JA, Sinclair LC, Sonderhouse L, Swann WC, Yao J, Ye J, and Zhang X. Frequency ratio measurements at 18-digit accuracy using an optical clock network. eng. Nature (London) 2021; 591:564–9
22. Bandi TN. A Comprehensive Overview of Atomic Clocks and their Applications. Biology, Engineering, Medicine and Science Reports 2023 Feb; 9:1–10.

DOI: 10.5530/bems.9.1.1. Available from: https://www.bemsreports.org/index.php/bems/article/view/128

23. Terrien J. News from the International Bureau of Weights and Measures. Metrologia 1968 Jan; 4:41. DOI: 10.1088/0026-1394/4/1/006. Available from: https://dx.doi.org/10.1088/0026-1394/4/1/006
24. Hu H and Wei N. A study of GPS jamming and anti-jamming. *2009 2nd International Conference on Power Electronics and Intelligent Transportation System (PEITS)*. Vol. 1. 2009 :388–91. DOI: 10.1109/PEITS.2009.5406988
25. Knappe S. Emerging Topics: MEMS Atomic Clocks. en. 3. Elsevier (Netherlands), NL, 2007. Available from: https://tsapps.nist.gov/publication/get_pdf.cfm?pub_id=50424
26. Marlow BLS and Scherer DR. A Review of Commercial and Emerging Atomic Frequency Standards. IEEE Transactions on Ultrasonics, Ferroelectrics, and Frequency Control 2021; 68:2007–22. DOI: 10.1109/TUFFC.2021.3049713
27. Porfyrakis K and Laird EA. Keeping perfect time with caged atoms. IEEE Spectrum 2017; 54:34–9. DOI: 10.1109/MSPEC.2017.8118481
28. Laeter JR de, Böhlke JK, Bièvre PD, Hidaka H, Peiser HS, Rosman KJR, and Taylor PDP. Pure and Applied Chemistry 2003; 75:683–800. DOI: doi:10.1351/pac200375060683. Available from: https://doi.org/10.1351/pac200375060683
29. Harding RT, Zhou S, Zhou J, Lindvall T, Myers WK, Ardavan A, Briggs GAD, Porfyrakis K, and Laird EA. Spin Resonance Clock Transition of the Endohedral Fullerene $^{15}N@C_{60}$. eng. Physical review letters 2017; 119:140801–
30. Green M. Spin resonance measurements of the clock molecule 15N@C60. PhD thesis. Lancaster University, 2025
31. Boča R. Zero-field splitting in metal complexes. Coordination Chemistry Reviews 2004; 248:757–815. DOI: https://doi.org/10.1016/j.ccr.2004.03.001. Available from: https://www.sciencedirect.com/science/article/pii/S0010854504000463
32. Ashbrook SE and Wimperis S. Quadrupolar coupling: An introduction and crystallographic aspects. RE Wasylishen, SA Ashbrook und S. Wimperis (Editoren), NMR of Quadrupolar Nuclei in Solid Materials, Kapitel 2007; 3:45–61
33. Marinov MB, Ganev B, Djermanova N, and Tashev TD. Analysis of Sensors Noise Performance Using Allan Deviation. *2019 IEEE XXVIII International Scientific Conference Electronics (ET)*. 2019 :1–4. DOI: 10.1109/ET.2019.8878552
34. Allan DW. IEEE Transactions on Instrumentation and Measurement. Should the classical variance be used as a basic measure in standards metrology? 1987; IM-36

35. Riehle F. Characterisation of Amplitude and Frequency Noise. *Frequency Standards*. John Wiley Sons, Ltd, 2003. Chap. 3:47–79. DOI: https://doi.org/10.1002/3527605991.ch3. eprint: https://onlinelibrary.wiley.com/doi/pdf/10.1002/3527605991.ch3. Available from: https://onlinelibrary.wiley.com/doi/abs/10.1002/3527605991.ch3
36. Chavhan GB, Babyn PS, Thomas B, Shroff MM, and Haacke EM. Principles, Techniques, and Applications of T2*-based MR Imaging and Its Special Applications. RadioGraphics 2009; 29. PMID: 19755604:1433–49. DOI: 10.1148/rg.295095034. eprint: https://doi.org/10.1148/rg.295095034. Available from: https://doi.org/10.1148/rg.295095034
37. Deng Y, Pandian RP, Ahmad R, Kuppusamy P, and Zweier JL. Application of magnetic field over-modulation for improved EPR linewidth measurements using probes with Lorentzian lineshape. Journal of Magnetic Resonance 2006; 181:254–61. DOI: https://doi.org/10.1016/j.jmr.2006.05.010. Available from: https://www.sciencedirect.com/science/article/pii/S1090780706001418
38. Robinson B, Mailer C, and Reese A. Linewidth Analysis of Spin Labels in Liquids: I. Theory and Data Analysis. Journal of Magnetic Resonance 1999; 138:199–209. DOI: https://doi.org/10.1006/jmre.1999.1737. Available from: https://www.sciencedirect.com/science/article/pii/S1090780799917378
39. Williams F. Electron Paramagnetic Resonance: Elementary Theory and Practical Applications, Second Edition (John A. Weil and James R. Bolton). eng. Journal of chemical education 2009; 86:33–
40. Vitanov N, Shore B, Yatsenko L, Böhmer K, Halfmann T, Rickes T, and Bergmann K. Power broadening revisited: theory and experiment. Optics Communications 2001; 199:117–26. DOI: https://doi.org/10.1016/S0030-4018(01)01495-X. Available from: https://www.sciencedirect.com/science/article/pii/S003040180101495X
41. Goldfarb D and Stoll S. EPR spectroscopy : fundamentals and methods. eng. Chichester, West Sussex, England, 2018 - 2018
42. Bagguley D. The echo phenomenon. Pulsed Magnetic Resonance–NMR, ESR, and Optics: A Recognition of EL Hahn 1992 :5–54
43. Available from: https://www.thinksrs.com/downloads/pdfs/applicationnotes/AboutLIAs.pdf
44. Kaszynski R and Piskorowski J. Bessel Filters with Varying Parameters. *2005 IEEE Instrumentationand Measurement Technology Conference Proceedings*. Vol. 1. 2005 :757–61. DOI: 10.1109/IMTC.2005.1604219
45. Mehdizadeh M, Ishii T, Hyde J, and Froncisz W. Loop-Gap Resonator: A Lumped Mode Microwave Resonant Structure. IEEE Transactions on

Microwave Theory and Techniques 1983; 31:1059–64. DOI: 10.1109/TMTT.1983.1131661

46. Froncisz W and Hyde JS. The loop-gap resonator: a new microwave lumped circuit ESR sample structure. Journal of Magnetic Resonance (1969) 1982; 47:515–21
47. Mett RR, Sidabras JW, and Hyde JS. Uniform radio frequency fields in loop-gap resonators for EPR spectroscopy. eng. Applied magnetic resonance 2007; 31:573–89
48. Bartoli M, Noferi N, Reatti A, and Kazimierczuk M. Modeling Litz-wire winding losses in high-frequency power inductors. *PESC Record. 27th Annual IEEE Power Electronics Specialists Conference*. Vol. 2. 1996 :1690–1696 vol.2. DOI: 10.1109/PESC.1996.548808
49. Wang S, Rooij M de, Odendaal W, Wyk J van, and Boroyevich D. Reduction of high-frequency conduction losses using a planar litz structure. IEEE Transactions on Power Electronics 2005; 20:261–7. DOI: 10.1109/TPEL.2004.843022
50. Etemadrezaei M and Lukic SM. Multilayer Tubular Conductor for High Q-Factor Wireless Power Transfer System Resonators. IEEE Transactions on Industry Applications 2016; 52:4170–8. DOI: 10.1109/TIA.2016.2574772
51. Yordanov ND and Christova A. DPPH as a primary standard for quantitative EPR spectrometry. eng. Applied magnetic resonance 1994; 6:341–5
52. Friis H. Noise Figures of Radio Receivers. Proceedings of the IRE 1944; 32:419–22. DOI: 10.1109/JRPROC.1944.232049
53. Rinard GA, Quine RW, Harbridge JR, Song R, Eaton GR, and Eaton SS. Frequency Dependence of EPR Signal-to-Noise. eng. Journal of magnetic resonance (1997) 1999; 140:218–27
54. Ruoff R, Tse DS, Malhotra R, and Lorents DC. Solubility of fullerene (C60) in a variety of solvents. The Journal of Physical Chemistry 1993; 97:3379–83